INTERNATIONAL JOURNAL OF MECHANICAL SCIENCES

IMPACT FACTOR: 2.884

ISSN: 0020-7403

PUBLISHER: ELSEVIER UK

ACCEPTED MARCH 9TH 2018

FLOW VISUALIZATION USING HEAT LINES FOR UNSTEADY RADIATIVE HYDROMAGNETIC MICROPOLAR CONVECTION FROM A VERTICAL SLENDER HOLLOW CYLINDER

G. Janardhana Reddy[1, *], Bhaskerreddy Kethireddy[1] and **O. Anwar Bég[2]**

[1]*Department of Mathematics, Central University of Karnataka, Kalaburagi, India-585367*

[2]*Fluid Mechanics, Aeronautical and Mechanical Engineering, Department, School of Computing, Science and Engineering, University of Salford, Manchester M54WT, UK*

* *Corresponding author - Email:* janardhanreddy.nitw@gmail.com

ABSTRACT

The present study aims to investigate the thermal radiation heat transfer effect on unsteady magnetohydrodynamic (MHD) flow of micropolar fluid over a uniformly heated vertical hollow cylinder using Bejan's heat function concept. The normalized conservation equations emerge as a system of time-dependent non-linear coupled partial differential equations. Under appropriate wall and free stream conditions these equations are solved with an efficient unconditionally stable implicit scheme of Crank-Nicolson type. Important thermo-physical parameters featured include the magnetic body force parameter (M), Grashof (free convection) parameter (Gr), Eringen micropolar material parameter (K), Prandtl number (Pr), conjugate heat transfer parameter (P) and radiative-conductive Rosseland parameter (N), are analyzed on the flow-field with ranges 0-3, 10^5-10^6, 0-1.2, 0.7-7.0, 0-0.5 and 0-15, respectively. The time-histories of average values of momentum and heat transport coefficients, as well as the steady-state flow variables are presented for selected values of these non-dimensional parameters. With elevation in magnetic parameter or radiation parameter, the time taken for the flow-field variables to attain the *time-independent state* increases. The dimensionless thermal radiative heat function values are closely correlated with the overall rate of heat transfer on the outer hot cylindrical wall. Bejan's heat flow visualization implies that the thermal radiative heat function contours are compact in the neighbourhood of leading edge of the boundary layer on the outer hot cylindrical wall. Increasing radiation or magnetic parameter values result in an increase in the deviation of heat lines from the hot wall. Also, the heatlines are observed to depart slightly away from the hot wall with greater values of vortex viscosity. Furthermore, the deviations of flow variables from the hot wall for a micropolar fluid are significant compared to the Newtonian fluid (vanishing micropolar vortex viscosity).

KEYWORDS: *Micropolar fluid; MHD; vertical slender hollow cylinder; heat function; finite difference method; nonlinear convection; thermal radiation; enrobing flows.*

NOMENCLATURE

B_0 applied magnetic field
B magnetic flux
$\overline{C_f}$ dimensionless average momentum transport coefficient
E electric field
Gr Grashof number
H magnetic field
J current density
j microinertia per unit mass
c_p specific heat (isobaric)
g acceleration due to gravity
K dimensionless vortex viscosity (Eringen micropolar material parameter)
k_1 vortex viscosity
k_f, k_s thermal conductivity of the fluid and the solid cylinder, respectively
M magnetic body force parameter
P conjugate heat transfer parameter
N conduction-radiation parameter (Rosseland number)
$\overline{Nu}$ dimensionless average heat transport coefficient
r radial coordinate
r_i radius of the inner cylinder
Pr Prandtl number
R dimensionless radial coordinate
p fluid pressure
q_r radiative heat flux
X dimensionless axial coordinate
U velocity vector
U, V dimensionless velocity components in (X, R) coordinate system
r_o radius of the outer cylinder
S micro-rotation vector
S' micro-rotation of the fluid in the xr-plane
S dimensionless micro-rotation of the fluid
T_0' temperature of the inner cylinder
x axial coordinate
L length of the cylinder
u, v velocity components in (x, r) coordinate system
t' dimensional time
t dimensionless time
τ_{ij} stress tensor
T' fluid temperature

Greek symbols

θ dimensionless temperature
β_T volumetric coefficient of thermal expansion
κ^* mean absorption coefficient

γ spin gradient viscosity
ρ density
σ^* Stefan-Boltzmann constant
μ dynamic viscosity of the fluid
Ω' heat function
Ω dimensionless heat function
υ kinematic viscosity of the fluid
σ electrical conductivity of the fluid
α thermal diffusivity
ψ dimensionless stream function

Subscripts

l, m grid levels in *(X, R)* coordinate system
w wall conditions
∞ ambient conditions

Superscripts

n time level

1. INTRODUCTION

Unsteady natural convection flows of viscous incompressible fluids from the *exterior* of solid bodies feature in an extensive range of applications including thermal coating processes, geophysical transport, fire dynamics and solar collector systems. Both laminar and turbulent flows from cylindrical bodies are a significant sub-branch of such problems and frequently feature boundary-layer phenomena. Sparrow and Gregg [1] conducted an early study of natural convection boundary layer flow from a uniformly heated vertical cylinder. Lee *et al*. [2] studied a similar problem with power-law variation in temperature along a thin vertical cylinder i.e. non-isothermal free convection flow. These investigations were confined to Newtonian fluids. However rheological fluids are invariably encountered in real polymeric materials processing systems and require constitutive formulations that do not conform to the classical Navier-Stokes model. Furthermore, in numerous investigations, the *wall conduction resistance* in the case of convection heat transfer between a solid cylinder wall and fluid flow is ignored i.e. there is no conduction from the solid cylinder wall. However, in many industrial applications, the interfacial temperature is needed since the physical characteristics of heat transfer are influenced by the temperature dissimilarities between the bulk flow and the solid interface. Therefore, the convection in the fluid and the conduction in the solid interface should be determined simultaneously. This type of convective flow heat transfer is known as a conjugate heat transfer (CHT) process and arises in rocket chamber film cooling, energy conservation, combustion of plastics, thermal barrier coating (TBC) of gas turbine components etc. Many researchers have widely studied this type of CHT research problems [3-6], with the help of mathematical modelling for different flow geometries, although these have been invariably restricted to Newtonian fluids. Very few non-Newtonian conjugate heat transfer simulations have been reported however. Rani and Reddy [7] examined the influence of Dufour and Soret effects on non-Newtonian fluid flow

from a vertical cylinder. Recently Hirschhorn *et al.* [8] investigated the non-Newtonian magnetohydrodynamic (MHD) flow from a plate with slip boundary conditions.

There is a diverse spectrum of non-Newtonian fluid theories available in the literature. The vast majority modify the Navier-Stokes formulation with extra stress tensors to accommodate different rheological phenomena including shear thinning/thickening, relaxation, retardation, memory etc. However, a more sophisticated family of models exhibit microstructure and these belong to a class of fluids with an asymmetric stress tensor. These types of fluids have a wider range of application in engineering sciences since they can capture micro-rheological effects associated with suspended particles. They are applicable to biological systems, geological processes, lubrication (tribology), polymers, liquid crystals, plasmas etc. Among these so-called "polar theories" the most comprehensive was developed by Eringen [9] and termed *micro-morphic fluid mechanics.* A subset of this elegant theory was later developed also developed by Eringen [10] and termed *micropolar* fluid theory, wherein a gyration parameter and micro-rotation vector is introduced additionally to the classical velocity field to study the kinematics of micro-rotation. A further modification for thermal properties was later presented again by Eringen [11]. Micropolar fluid dynamics has successfully addressed complex fluids including liquid crystals, colloidal solutions, lubricants, ferrofluids, smart fluids, polymeric fluids, animal blood etc. Representative studies of micropolar fluids with multiple physical effects include biophysical transport phenomena [12-14], magnetohydrodynamics (MHD) flows [15-16] and geomechanics [17]. Another interesting application i.e. channel cooling, was considered by Prathap Kumar *et al*. [18] in which fully developed micropolar convection was analysed in a vertical channel. An excellent review of the applications of micropolar fluids has been presented by Ariman *et al.* [19]. Recently, Tetbirt *et al.* [20] studied the hydromagnetic micropolar flow in a vertical channel with MHD effect.

The above studies have generally considered thermal conduction and convection modes of heat transfer in micropolar fluid mechanics. However, in high temperature applications (e.g. rocket channel cooling, materials processing etc.) *thermal radiative heat transfer* becomes substantial. Radiative transfer also features prominently in glass synthesis processes, combustor design, solar energy engineering, nuclear reactor thermo-hydraulics, laser ablation of materials. When fluids have electrically-conducting properties then magnetohydrodynamic (MHD) effects are also invoked. These may feature Lorentzian body forces, magnetic induction, Ohmic dissipation, Hall currents, ionslip effects, Alfven waves etc. Radiative magnetohydrodynamic coating fabrication systems therefore require the simultaneous consideration of MHD and thermal radiative effects in addition to viscous flow, thermal conduction and convection.

A careful inspection of the scientific and technical literature has identified that very scant attention has been directed towards *unsteady hydromagnetic micropolar fluid flow from a radiative vertical slender cylinder, which is of great interest in magnetic thermal enrobing flows in materials operations*. Therefore, in the present article, a theoretical and numerical study of micropolar fluid flow over a uniformly heated vertical thin hollow cylinder in the boundary layer region is presented. The temperature of the inner cylindrical wall is maintained uniformly and is greater than the surrounding fluid temperature. The temperature of the outer cylinder wall is resolved by the conjugate solution of the time-independent state energy equation of the solid and fluid flow. The transitory effects of the micropolar fluid flow are studied for the momentum and heat transport coefficients for different control parameters and compared with the Newtonian fluid flow. The non-linear boundary value problem is solved with the Crank-Nicolson implicit finite difference method and validation is included with the available existing results in the literature.

Usually, the numerical simulation of fluid dynamics problems are analysed only with the help of popular visualization techniques such as streamlines, velocity vectors and isotherms. Apart from streamlines, the other two can be simulated directly from the primary variables using suitable plotting softwares. In a given domain isotherms will contribute to illustrate the temperature distribution. However, by utilizing them a visualization of the direction and heat transfer intensity is not possible. In particular, in thermal convection flows, the direction of heat flux is not normal to temperature contours. Also, isotherms are a proper heat transfer visualization tools only in the field of conduction (where, in fact, they have been invented) because only there they are locally orthogonal to the true direction of energy flow. Researchers have developed different novel visualization tools to explain the flow physics and behavior of the system. Kimura and Bejan [21] and Bejan [22] initiated the heat line concept of flow visualization. Heatlines help in visualization of the energy flow in the domain. Also, heat lines provide an excellent mechanism for visualizing the intensity of heat transfer and furnish well-defined pathways for the energy transfer to occur from hot to cold walls. Mahmud and Fraser [23] introduced an alternative visualization technique for convective heat transfer called energy streamlines. Transport of different other forms of energy like chemical, electrical, magnetic, thermal, potential and kinetic energy are considered in the energy streamlines. Hooman [24] initiated another novel visualization tool called energy flux vectors which are used to visualize the flow of energy. Further, the energy flux vectors bridge the gap between the heatlines and energy streamlines, each of which extensively used for visualization purpose. As these vectors are tangent to the heatlines and represents the flow of energy in a 2D domain. This technique (energy flux vectors) can be applied for situations where heatlines cannot be applied, namely, unsteady problems, 3D flows, and energy equations with source terms. Further, by applying the energy flux vectors, the difficulty of formulating the suitable boundary conditions for heat lines and energy streamlines can be overcome. However, quantitative estimates of heat transfer cannot be obtained using this technique(Mahapatra *et al*.[25]). Similarly, Mahapatra *et al.* [26], studied the natural convection in alternately active bi-heater located at the bottom of an enclosure for different switchover time period. Also, they explained the energy flux vectors and streamlines at different time zones. More details about these novel flow visualization techniques can be found in (Mahapatra *et al*.[25]). However, in the present study the heat lines are discussed for steady-state case only. For cylindrical enclosures, Aggarwal and Manhapra [27] employed the heat lines concept under steady-state condition for the natural convective heat transfer process. In a similar way, Rani and Reddy [28] studied the heat lines for couple stress thermal convection from a vertical cylinder. Later, couple stress thermosolutal convection along a vertical cylinder was scrutinized by Rani *et al*. [29] using the concept of heat line and also mass line visualization. Using the same idea, recently Das and Basak [30] analysed the rate of heat transfer at different zones within enclosures involving discrete heaters. Further elaboration on the heat line methodology in thermal convection flows has been provided by Morega [31-32]. Recent studies on heat lines can be found in [33-35]. Thusfar their remains a rather sparse literature available however deploying the heat lines concept. This, in part, has motivated the present investigation wherein *for the first time*, an attempt has been made to visualize the flow behaviour for thermal radiation and magnetohydrodynamic effects using the heat line function concept.

2. MATHEMATICAL MODELLING

Transient two-dimensional laminar buoyancy-driven (natural convection) electrically – conducting micropolar boundary layer flow from a radiating slender cylinder of outer radius r_0

under the action of a transversely applied (radial) static magnetic field B_0, is considered. The physical model is depicted in **Fig. 1**. A rectangular coordinate system is selected, in which the axial coordinate (*x*-axis) is orientated from the base of the cylinder, while the radial coordinate (*r*-axis) is directed normal to the *x*-axis. The neighboring fluid temperature is considered to be stationary and similar to that of free stream temperature T'_∞. The temperature of the interior wall of the cylinder is preserved at a uniform value of T'_0, where $T'_0 > T'_\infty$. At the outset, i.e. $t' = 0$ the temperature T'_∞ is uniform for the outer cylinder and the surrounding fluid. Later ($t' > 0$), the temperature of the outer vertical cylinder is augmented to the fluid-solid interface temperature T'_w ($> T'_\infty$) and preserved uniformly thereafter. This temperature T'_w is resolved by the conjugate solution of the time-independent state thermal equation of the solid and the governing equations of the micropolar fluid flow and is explained later. The radiative heat flux in the energy equation is described by using Rosseland's approximation which simplifies the general radiative transfer equation into a diffusion flux algebraic formulation, generally valid for optically thin flows. Hall current, ionslip, magnetic induction and optical thickness effects are neglected. The relevant conservation equations for mass and momentum (linear and angular) may be presented as follows:

Law of conservation of mass:

$$\frac{\partial(ru)}{\partial x} + \frac{\partial(rv)}{\partial r} = 0 \tag{1}$$

Law of conservation of linear momentum:

$$\rho\left[\frac{\partial \mathbf{U}}{\partial t'} + (\mathbf{U}.\nabla)\mathbf{U}\right] = -\rho g - \nabla p + (\mu + k_1)\nabla^2\mathbf{U} + k_1\nabla\times\mathbf{S} + (\mathbf{J}\times\mathbf{B}) \tag{2}$$

where, **J** and **B** are given by Ohm's law and Maxwell's equations, namely,

$\nabla\times\mathbf{E} = 0,\ \nabla\times\mathbf{H} = 4\pi\mathbf{J},\ \nabla\times\mathbf{B} = 0,\ \mathbf{J} = \sigma[\mathbf{E} + \mathbf{U}\times\mathbf{B}]$

Law of conservation of angular momentum:

$$\rho j\left[\frac{\partial \mathbf{S}}{\partial t'} + (\mathbf{U}.\nabla)\mathbf{S}\right] = -2k_1\mathbf{S} + k_1\nabla\times\mathbf{U} - \gamma(\nabla\times\nabla\times\mathbf{S}) \tag{3}$$

Here the following notation applies: $\boldsymbol{U}$ is the velocity vector, $\boldsymbol{H}$ is the magnetic field vector, $\boldsymbol{S}$ is the microrotation vector, j is the microinertia constant, k_1 is the vortex viscosity coefficient, **J** is the current density, γ is the spin gradient viscosity, $\boldsymbol{E}$ is the electric field vector, **B** is the magnetic flux vector and σ is the electrical conductivity of the fluid. It is presumed that the magnetic Reynolds number is very small. Therefore, the interaction of the induced axial magnetic field with the motion of electrically-conducting micropolar fluid flow is expected to be minuscule compared to the interaction of the applied magnetic field. Further, no external electric field is applied. With these assumptions, the Lorentzian magnetic body force term defined by the vector cross product $\boldsymbol{J}\times\boldsymbol{B}$ in the momentum equation (2) reduces to $-\sigma B_0^2 u$ where B_0 is the strength of the transverse magnetic field. Using Boussinesq's approximation Eqns. (2) & (3) can be re-written as follows:

$$\rho\left(\frac{\partial u}{\partial t'} + u\frac{\partial u}{\partial x} + v\frac{\partial u}{\partial r}\right) =$$

$$(\mu + k_1)\frac{1}{r}\frac{\partial}{\partial r}\left(r\frac{\partial u}{\partial r}\right) + k_1\frac{\partial S'}{\partial r} + \rho g\beta_T(T' - T'_\infty) - \sigma B_0^2 u \quad (4)$$

$$\rho j\left(\frac{\partial S'}{\partial t'} + u\frac{\partial S'}{\partial x} + v\frac{\partial S'}{\partial r}\right) =$$

$$\gamma\frac{1}{r}\frac{\partial}{\partial r}\left(r\frac{\partial S'}{\partial r}\right) - k_1\left(2S' + \frac{\partial u}{\partial r} - \frac{\partial v}{\partial x}\right) \quad (5)$$

The stress tensors related to micropolar fluid theory are given by [9-11]:

$$\tau_{ij} = -p\delta_{ij} + (2\mu + k_1)d_{ij} + k_1\varepsilon_{ijm}[\omega_m - \mathrm{S}_m] \quad (6)$$

$$m_{ij} = \alpha_1(\nabla.\mathbf{S})\delta_{ij} + \beta_1 \mathrm{S}_{i,j} + \gamma \mathrm{S}_{j,i} \quad (7)$$

Here δ_{ij}, d_{ij}, ω_m and S_m represent respectively the Kronecker symbol, components of rate of strain, vorticity vector and micro-rotation vector, ε_{ijm} denotes the Levi-Civita symbol, the material constants (α_1, β_1, γ) are the gyro-viscosity coefficients and a comma in the suffixes denotes covariant differentiation. The parameters α_1, β_1, γ, μ, k_1 are constrained by the following inequalities:

$$k_1 \geq 0;\ 2\mu + k_1 \geq 0;\ \gamma \geq 0;\ |\beta_1| \leq \gamma;\ 3\alpha_1 + \beta_1 + \gamma \geq 0. \quad (8)$$

Law of conservation of energy (heat):

$$\frac{\partial T'}{\partial t'} + u\frac{\partial T'}{\partial x} + v\frac{\partial T'}{\partial r} = \frac{\alpha}{r}\frac{\partial}{\partial r}\left(r\frac{\partial T'}{\partial r}\right) - \frac{1}{\rho c_p}\frac{1}{r}\frac{\partial}{\partial r}(rq_r) \quad (9)$$

Using Rosseland's diffusion approximation, the heat flux q_r is given by (Brewster [36])

$$q_r = -\frac{4\sigma^*}{3\kappa^*}\frac{\partial T'^4}{\partial r} \quad (10)$$

By Taylor series, the temperature T'^4 about T'_∞ is given by

$$T'^4 \cong 4(T'T'^3_\infty) - 3(T'^4_\infty) \quad (11)$$

In view of Eqns. (10) and (11), Eqn. (9) reduces to:

$$\frac{\partial T\prime}{\partial t\prime} + u\frac{\partial T\prime}{\partial x} + v\frac{\partial T\prime}{\partial r} = \frac{\alpha}{r}\frac{\partial}{\partial r}\left(r\frac{\partial T\prime}{\partial r}\right) + \left(\frac{16\sigma^* T'^3_\infty}{3\rho c_p \kappa^*}\right)\frac{1}{r}\frac{\partial}{\partial r}\left(r\frac{\partial T'}{\partial r}\right) \quad (12)$$

The initial and boundary conditions are prescribed as follows:

$$t' \leq 0: T' = T'_\infty,\ S' = 0, u = 0, v = 0 \qquad \forall\ x \text{ and } r$$

$$t' > 0: T' = T'_w,\ S' = -\frac{1}{2}\frac{\partial u}{\partial r}, u = 0, v = 0 \qquad \text{at } r = r_0$$

$$T' = T'_\infty,\ S' = 0, u = 0, v = 0 \qquad \text{at } x = 0$$

$$T' \to T'_\infty,\ S' \to 0, u \to 0, v \to 0 \qquad \text{as } r \to \infty \quad (13)$$

Here T'_w is the *fluid-solid interface temperature* and is given by (Chang [37]):

$$T'_w = T'(x,\ r_0) = \ r_0 \frac{k_f}{k_s} \ln\left(\frac{r_0}{r_i}\right) \frac{\partial T'(x,r_0)}{\partial r} + T'_0 \qquad \text{at } r = \ r_0 \tag{14}$$

To render the mathematical model as non-dimensional and thereby facilitate numerical solutions, the following dimensionless quantities are now invoked:

$$\theta = \frac{T'-T'_\infty}{T'_0-T'_\infty},\ P = \ \frac{k_f}{k_s}\ln\left(\frac{r_0}{r_i}\right),\ Gr = \frac{g\beta_T r_0^3(T'_0-T'_\infty)}{\upsilon^2},\ U = Gr^{-1/2}\frac{ur_0}{\upsilon},\ V = Gr^{-1/2}\frac{vr_0}{\upsilon},\ t = Gr^{1/2}\frac{\upsilon t'}{r_0^2},\ X = \frac{x}{r_0},\ Pr = \frac{\upsilon}{\alpha},\ R = \frac{r}{r_0},\ S = Gr^{-1/2}\frac{S'r_0^2}{\upsilon}, K = \frac{k_1}{\upsilon\rho},\ j = r_0^2,\ \gamma = (\mu + k_1/2)j = (1+K/2)\mu j,\ \alpha = \frac{k_f}{\rho c_p}, M = \frac{\sigma B_0^2 r_0^2}{\upsilon\rho},\ N = \frac{\kappa^* k_f}{4\ \sigma^* T'^3_\infty} \tag{15}$$

Here all parameters are defined in the nomenclature. Implementing Eqn. (15) in Eqns. (1), (4), (5), (12) and also in Eqn. (13), the following normalized, coupled, nonlinear partial differential equations (PDEs) emerge:

$$\frac{\partial U}{\partial X} + \frac{\partial V}{\partial R} + \frac{V}{R} = 0 \tag{16}$$

$$\frac{\partial U}{\partial t} + U\frac{\partial U}{\partial X} + V\frac{\partial U}{\partial R} = \theta + \left(\frac{1+K}{Gr^{1/2}}\right)\left(\frac{\partial^2 U}{\partial R^2} + \frac{1}{R}\frac{\partial U}{\partial R}\right) + \frac{K}{Gr^{1/2}}\frac{\partial S}{\partial R} - MU \tag{17}$$

$$\frac{\partial S}{\partial t} + U\frac{\partial S}{\partial X} + V\frac{\partial S}{\partial R} = \left(\frac{1+K/2}{Gr^{1/2}}\right)\left(\frac{\partial^2 S}{\partial R^2} + \frac{1}{R}\frac{\partial S}{\partial R}\right) - \frac{K}{Gr^{1/2}}\left(2S + \frac{\partial U}{\partial R} - \frac{\partial V}{\partial X}\right) \tag{18}$$

$$\frac{\partial \theta}{\partial t} + U\frac{\partial \theta}{\partial X} + V\frac{\partial \theta}{\partial R} = \frac{1}{PrGr^{1/2}}\left(1 + \frac{4}{3N}\right)\left(\frac{\partial^2 \theta}{\partial R^2} + \frac{1}{R}\frac{\partial \theta}{\partial R}\right) \tag{19}$$

$$\begin{aligned}
&t \le 0: \theta = 0, S = 0, U = 0, V = 0 && \forall\ X \text{ and } R \\
&t > 0: \theta - 1 = P\frac{\partial \theta}{\partial R},\ S = \frac{-1}{2}\frac{\partial U}{\partial R},\ U = 0,\ V = 0 && \text{at } R = 1 \\
&\qquad \theta = 0,\ S = 0,\ U = 0,\ V = 0 && \text{at } X = 0 \\
&\qquad \theta \to 0,\ S \to 0,\ U \to 0,\ V \to 0 && \text{as } R \to \infty
\end{aligned} \tag{20}$$

3. FINITE DIFFERENCE NUMERICAL SOLUTION PROCEDURE

To solve the normalized time-dependent PDEs. (16) - (19) under boundary conditions (20), an unconditionally stable finite difference iteration scheme of Crank-Nicolson type is employed. The finite difference equations to the above Eqs. (16), (17), (18) and (19) are as follows:

$$\frac{U_{l,m}^{n+1} - U_{l-1,m}^{n+1} + U_{l,m}^{n} - U_{l-1,m}^{n}}{2\Delta X} + \frac{V_{l,m}^{n+1} - V_{l,m-1}^{n+1} + V_{l,m}^{n} - V_{l,m-1}^{n}}{2\Delta R} + (JR)V_{l,m}^{n+1} = 0 \tag{21}$$

$$\frac{U_{l,m}^{n+1}-U_{l,m}^{n}}{\Delta t}+\frac{U_{l,m}^{n}}{2\Delta X}\left(U_{l,m}^{n+1}-U_{l-1,m}^{n+1}+U_{l,m}^{n}-U_{l-1,m}^{n}\right)+\frac{V_{l,m}^{n}}{4\Delta R}\left(U_{l,m}^{n+1}-U_{l,m-1}^{n+1}+U_{l,m}^{n}-U_{l,m-1}^{n}\right)$$
$$=\frac{\theta_{l,m}^{n+1}+\theta_{l,m}^{n}}{2}+\left(\frac{1+K/2}{Gr^{1/2}}\right)(JR)\left(\frac{U_{l,m+1}^{n+1}-U_{l,m-1}^{n+1}+U_{l,m+1}^{n}-U_{l,m-1}^{n}}{4(\Delta R)}\right)+M\frac{\left(U_{l,m}^{n+1}+U_{l,m}^{n+1}\right)}{2}$$
$$\left(\frac{1+K/2}{Gr^{1/2}}\right)\left(\frac{U_{l,m+1}^{n+1}-2U_{l,m}^{n+1}+U_{l,m-1}^{n+1}+U_{l,m+1}^{n}-2U_{l,m}^{n}+U_{l,m-1}^{n}}{2(\Delta R)^{2}}\right)+\left(\frac{K}{Gr^{1/2}}\right)\left(\frac{S_{l,m+1}^{n+1}-S_{l,m-1}^{n+1}+S_{l,m+1}^{n}-S_{l,m-1}^{n}}{4(\Delta R)}\right) \quad (22)$$

$$\frac{S_{l,m}^{n+1}-S_{l,m}^{n}}{\Delta t}+\frac{S_{l,m}^{n}}{2\Delta X}\left(S_{l,m}^{n+1}-S_{l-1,m}^{n+1}+S_{l,m}^{n}-S_{l-1,m}^{n}\right)+\frac{V_{l,m}^{n}}{4\Delta R}\left(S_{l,m}^{n+1}-S_{l,m-1}^{n+1}+S_{l,m}^{n}-S_{l,m-1}^{n}\right)$$
$$=\left(\frac{1+K/2}{Gr^{1/2}}\right)$$
$$\left(\frac{S_{l,m+1}^{n+1}-2S_{l,m}^{n+1}+S_{l,m-1}^{n+1}+S_{l,m+1}^{n}-2S_{l,m}^{n}+S_{l,m-1}^{n}}{2(\Delta R)^{2}}\right)+\left(\frac{1+\frac{K}{2}}{Gr^{1/2}}\right)(JR)\left(\frac{S_{l,m+1}^{n+1}-S_{l,m-1}^{n+1}+S_{l,m+1}^{n}-S_{l,m-1}^{n}}{4(\Delta R)}\right)-2\frac{K}{Gr^{1/2}}S_{l,m}^{n}-$$
$$\left(\frac{K}{Gr^{1/2}}\right)\left(\frac{U_{l,m+1}^{n+1}-U_{l,m-1}^{n+1}+U_{l,m+1}^{n}-U_{l,m-1}^{n}}{4(\Delta R)}\right)+\left(\frac{K}{Gr^{1/2}}\right)\left(\frac{V_{l+1,m}^{n+1}-V_{l,m}^{n+1}+V_{l+1,m}^{n}-V_{l,m}^{n}}{2(\Delta X)}\right) \quad (23)$$

$$\frac{\theta_{l,m}^{n+1}-\theta_{l,m}^{n}}{\Delta t}+\frac{U_{l,m}^{n}}{2\Delta X}\left(\theta_{l,m}^{n+1}-\theta_{l-1,m}^{n+1}+\theta_{l,m}^{n}-\theta_{l-1,m}^{n}\right)+\frac{V_{l,m}^{n}}{4\Delta R}\left(\theta_{l,m+1}^{n+1}-\theta_{l,m-1}^{n+1}+\theta_{l,m+1}^{n}-\theta_{l,m-1}^{n}\right)$$
$$=\left(\mathbf{1}+\frac{\mathbf{4}}{\mathbf{3}\boldsymbol{N}}\right)\left[\frac{\theta_{l,m+1}^{n+1}-2\theta_{l,m}^{n+1}+\theta_{l,m-1}^{n+1}+\theta_{l,m+1}^{n}-2\theta_{l,m}^{n}+\theta_{l,m-1}^{n}}{2PrGr^{1/2}(\Delta R)^{2}}\right]+(JR)\left[\frac{\theta_{l,m+1}^{n+1}-\theta_{l,m-1}^{n+1}+\theta_{l,m+1}^{n}-\theta_{l,m-1}^{n}}{4PrGr^{1/2}(\Delta R)}\right] \quad (24)$$

where $JR=\frac{1}{[1+(m-1)\Delta R]}$.

The computations are executed based on a rectangular finite difference mesh (grid) with $X_{max}=1$, $X_{min}=0$, $R_{max}=7$ and $R_{min}=1$ where R_{max} relates to $R=\infty$ which lies far away from the heat and momentum transport boundary layers.

3.1 Validation of the numerical code using grid independence study:

To optimize accuracy and compilation times, a grid-independency test has been conducted using four different grid sizes of 20 X 120, 30 X 180, 40 X 240, 50 X 300 and 60 X 360 and the values of the $\overline{C_f}$ and $\overline{Nu}$ on the boundary R = 1 are shown in **Table 1**. A regular grid is used for all cases. It is observed from **Table 1** that the 50 X 300 grid compared with 40 X 240 and 60 X 360 does not have any significant effect on the results of $\overline{C_f}$ and $\overline{Nu}$. Hence according to this observation, a uniform grid size of 50 X 300 is sufficiently accurate for this study with the mesh step distances of 0.02 and 0.02 in the axial and radial directions, respectively. Similarly, to produce a reliable result with respect to time, a grid-independent test has been performed for different time step sizes and is shown in **Table 2** wherein the time step size Δt ($t=n\Delta t, n=0,1,2,\ldots$) is fixed as 0.01.

The finite difference procedure begins by computing the solution for the thermal boundary layer Eqn. (24) and angular momentum boundary layer Eqn. (23), which yields the temperature and micro-rotation fields. Next the linear momentum boundary layer and mass conservation Eqns. (22) and (21) provide the solution for the linear velocity field. Equations (22) - (24) at the (n+1)th stage using the n^{th} stage known values are specified in the following tridiagonal form:

$$a_{l,m}\Phi_{l,m-1}^{n+1}+b_{l,m}\Phi_{l,m}^{n+1}+c_{l,m}\Phi_{l,m+1}^{n+1}=d_{l,m}^{n} \quad (25)$$

Here Φ signifies the time-dependent flow-field variables θ, S and U. Thus, Eqns. (22) - (24) at each interior grid point on a precise l-level comprise a system of tridiagonal equations. Such a complex system of tridiagonal equations is solved by the famous Thomas algorithm. The convergence criterion was chosen as 10^{-6} for all flow-field variables. The truncation error in the employed Crank-Nicolson method is $O(\Delta t^2 + \Delta X + \Delta R^2)$ and tends to zero as ΔR, ΔX and $\Delta t \rightarrow 0$. Further details of the Crank-Nicolson finite difference scheme are documented in Rani *et al*. [38].

4. RESULTS AND DISCUSSION

To study the unsteady behavior of simulated micropolar fluid flow-field variables, such as U, θ, and S, their values are illustrated at one location, which is adjacent to the hot cylindrical wall. The time-independent state velocity, temperature, and micro-rotation profiles are presented along with the radial coordinate at $X = 1.0$.

The computer-generated flow-field variables for the case of Newtonian fluids ($K = 0.0$) are similar to those of Lee *et al*. [2] for $P = M = N = 0.0$ and $Pr = 0.7$, and are illustrated in **Fig. 2**. Also, the local heat transfer rate result obtained by the current research work is compared with those of Heckel *et al.* [39] for a Newtonian fluid, and shown in **Table 3**. These results are found to be in good agreement. The influence of M (magnetic parameter) and N (radiation parameter) on the micropolar flow-field are analysed with fixed values of Prandtl number (Pr), Grashof number (Gr), vortex viscosity (K) and conjugate heat transfer parameter (P).

4.1 Flow variables

Velocity:

The simulated linear velocity (U) plotted against time (t) at a spatial location (1, 1.16) for different M and N is graphically shown in **Fig. 3**. The U profile is taken in the vicinity of the hot cylindrical wall. Evidently as N increases, the velocity is enhanced with time, attains a temporal peak, then marginally decreases, and finally, remains invariant with further progression in time. Similarly, the same transient behavior is noticed for M but the temporal peak is absent. Also, it is perceived that when $t << 1$, the conduction dominates the convection. Then the heat transport coefficient is swayed by the convection effect resulting in an escalation in velocities. Later before attaining the steady-state, the velocities are found to overshoot. Also, in the Fig. 3 it is observed that the transient U profile decreases as M or N increases. It is also observed that the time to attain the temporal peak upsurges as N increases. Also it is noticed that as M or N increase the time to accomplish the steady-state also increases, since a higher M value corresponds to greater retarding effect associated with the Lorentzian magnetic body force (greater resistance to the flow) and a higher N value allows higher thermal transport across the boundary. The same observation is tabulated in **Table 4**. Similarly, the transient characteristics of temperature and micro-rotation are illustrated in Figs. 5 and 7, respectively (described later). With the aid of Fig. 4, these velocity fluctuations of M and N are analyzed next. The solutions in the radial direction for the time-independent state U profile correspond to $X = 1.0$. Linear velocity commences with the no-slip boundary condition, reaches its peak and then decays to zero along the R coordinate satisfying the boundary condition ($U \rightarrow 0$ as $R \rightarrow \infty$). In the neighborhood of the hot wall, it is noted that the magnitude of non-dimensional axial velocity (U) is amplified as R rises from R_{min} (= 1). With increasing M or N, the time to reach the steady-state increases slightly. From Fig. 4, it is also apparent that the velocity decreases with increasing values of M or N. This implies that magnetic

field suppresses fluid velocity i.e. damps the flow field. This is due to the fact that the application of magnetic field to an electrically-conducting fluid gives rise to resistive force which is known as the Lorentz force. Also, the boundary layer thickness increases with increasing values of the magnetic parameter since the flow is decelerated. Here, the effect of N on the velocity profile can be considered. In a typical natural convection without radiative effects, the thermal term $\left(\frac{\partial^2\theta}{\partial R^2}+\frac{1}{R}\frac{\partial\theta}{\partial R}\right)$, which is conventionally positive, makes the convective term to be positive. With the radiative effect in this problem a higher value of N yields smaller convective term, resulting in a profile of low temperature at X = 1.0 (see Figs. 5 and 6) and, therefore, yields a lower velocity. Also Fig. 4 shows that the U profiles attain their peak value nearly at (1, 1.08).

Temperature:

Figure 5 depicts the impact of M and N on unsteady temperature profile (θ) against the time (t) at the location (1, 1.16). From this data, in the beginning for all values of N, the unsteady temperature profile is found to drastically increase with time, reaches the peak value, then decreases and again slightly increases, and finally attains the time-independent state asymptotically. A similar transient behavior is noticed for M but the temporal peak is not seen. For all values of M, the transient temperature curves initially coincide and then deviate from each other after some time. The time to attain temporal peak upsurges as N increases. Also from Fig. 5 it is noticed that as M or N are elevated, the time to accomplish the steady-state increases. It is also observed that the transient temperature value is boosted with greater M whereas it is depleted with increasing N. This tendency is also observed in Fig. 6 which depicts the steady-state non-dimensional θ-profile for the variation of M and N against R at X = 1.0. Here, the temperature profile initiates with the *solid-fluid interface hot wall temperature* and then monotonically decrease to zero ($\theta \rightarrow 0$) along the radial direction (R). It is noticed that the temperature increases with increasing M, while the reverse trend is observed for increasing N. As the value of N increases from 2 to 15 with fixed M (= 1.0), the temperature decreases markedly i.e. thermal conduction dominating radiation induces significant cooling. As a result, the thermal boundary layer thickness is decreased due to a rise in N values. Smaller M and larger N values give rise to thinner thermal boundary layers, since a smaller M value implies less-suppressed boundary layer flow, and a larger N value means smaller thermal convection.

Microrotation:

In Figure 7 the transient micro-rotation (S) values are plotted at the position (1, 1.16) against time for various values of M and N. Evidently transient micro-rotation S decreases with time, reach the temporal minimum, again increases and then reaches the asymptotic time-independent state. Furthermore the time to reach temporal minima for the transient micro-rotation, S increases, as M or N are increased. Moreover the time need to attain the steady-state upsurges as M or N amplifies.

The time-independent state S profile at X = 1.0 against the R for the variation of M and N are depicted in Fig. 8. In Fig. 8 it is noticed that in the neighborhood of the hot wall the S profiles start with negative values, slightly decreases, then increases and attains the peak value [i.e., in the interval $R \in (1.20, 1.30)$], and finally reaches to the no-slip boundary condition (S = 0) as the radial coordinate tends to R_{max}. Also, in the region $1<R<1.10$, as M or N increase the steady-state micro-rotation profile increases. In the neighborhood of the hot wall increasing magnetic field (M) leads to decrease in the velocity which causes an increase in S (refer to Fig. 4 and Eqns. 17-18).

4.2 Friction and heat transport coefficients

The average momentum and heat transport coefficients are significant parameters in heat transfer analysis due to their direct involvement in the convection process. The non-dimensional average momentum and heat transport coefficients for a micropolar fluid are given by:

$$\overline{C_f} = \int_0^1 \left(\frac{\partial U}{\partial R}\right)_{R=1} dX \tag{25}$$

$$\overline{Nu} = -\int_0^1 \left(\frac{\partial \theta}{\partial R}\right)_{R=1} dX \tag{26}$$

Figures 9-10 illustrate the distributions in $\overline{C_f}$ and $\overline{Nu}$ against time (t) covering various parametric values of M and N. The effect of various control parameters on $\overline{C_f}$ is revealed in Fig. 9. At first the $\overline{C_f}$ increases with t, and after a certain lapse of time, becomes independent of time throughout the transient period. This is probably due to the buoyancy-induced flow-field velocity being comparatively small at the initial time-dependent period, as plotted in Fig. 3, and the average momentum transport coefficient therefore remains low, as observed in Fig. 9. Also, it is seen that $\overline{C_f}$ decreases with augmenting values of M or N, a feature consistent with the time-dependent velocity profile in Fig. 3. The average heat transport coefficient ($\overline{Nu}$) for several values of M and N are graphically shown in Fig. 10. For all values of M and N, in the initial stages, $\overline{Nu}$ drastically decreases, then slightly increases and finally achieves the time-independent state. Initially the $\overline{Nu}$ curves coincide with each other and subsequently diverge after some time. Evidently in the starting time only heat conduction occurs, and dominates heat convection. From Fig. 4 it is also noteworthy that as M increases, the effect of the Lorentz force on the flow field decreases, and hence the flow velocity increases in the boundary layer region. This is associated with higher temperature gradients at the walls, resulting in higher heat transfer rates. Also, as N increases the rate of heat transfer increases.

4.3 Stream and heat functions

The fluid motion is simulated using the non-dimensional stream function ψ that satisfies the Eq. (16). The relationship between ψ, U, and V for two-dimensional flows is given by the Cauchy-Riemann equations:

$$U = \frac{1}{R}\frac{\partial \psi}{\partial R} \quad \text{and} \quad V = -\frac{1}{R}\frac{\partial \psi}{\partial X} \tag{27}$$

This yields:

$$\frac{\partial^2 \psi}{\partial X^2} + \frac{\partial^2 \psi}{\partial R^2} = R\frac{\partial U}{\partial R} - R\frac{\partial V}{\partial X} + U \tag{28}$$

Similarly, the heat function Ω' for the temperature is defined as:

$$\frac{\partial \Omega'}{\partial x} = \rho r v c_p (T' - T'_\infty) - k_f r \frac{\partial T'}{\partial r} - \left(\frac{16\sigma^* {T'_\infty}^3}{3k^*}\right)\left(r\frac{\partial T'}{\partial r}\right) \tag{29a}$$

$$-\frac{1}{r}\frac{\partial \Omega'}{\partial r} = \rho u c_p (T' - T'_\infty) \tag{29b}$$

It can be noted that Ω' satisfies the steady-state energy balance equation (12). The non-dimensional heat function $\Omega = \frac{\Omega'}{k_f(T_0' - T_\infty')r_0\left(1+\frac{4}{3N}\right)}$ makes the heat function dimensionless. The maximum value of this function equals the overall average heat transport coefficient on the hot wall [21, 40]. Eqns. (29a) and (29b) in terms of Ω can be rewritten as:

$$\frac{\partial \Omega}{\partial X} = \frac{PrGr^{1/2}(RV\theta)}{\left(1+\frac{4}{3N}\right)} - R\frac{\partial \theta}{\partial R} \tag{30a}$$

$$-\frac{\partial \Omega}{\partial R} = \frac{PrGr^{1/2}}{\left(1+\frac{4}{3N}\right)}(RU\theta) \tag{30b}$$

The above equations identically satisfy the time-independent state form of the heat conservation Eqn. (19). Using Eqns. 30a,b, one can obtain the following Poisson equation which gives heat function field as:

$$\frac{\partial^2 \Omega}{\partial X^2} + \frac{\partial^2 \Omega}{\partial R^2} = \frac{Pr}{\left(1+\frac{4}{3N}\right)}\left[R\frac{\partial (V\theta)}{\partial X} - R\frac{\partial (U\theta)}{\partial R} - U\theta\right] - R\frac{\partial^2 \theta}{\partial X \partial R} \tag{31}$$

The values of ψ, θ *and* Ω are calculated using central finite differences of second-order. The steady-state streamlines, isotherms and heat lines are presented in **Figs. 11a-11c**, respectively, for different values of the magnetic and conduction-radiation parameters, *M* and *N*. In each figure, the variation of *M* is shown between (i) and (ii); similarly, *N* between (ii) and (iii). For all control parameters, the variation in isotherms and heat lines occurs in the proximity of the hot cylindrical wall as compared to that of the streamlines. Fig. 11a indicates that the streamlines are moving slightly away from the hot wall and becoming denser with increasing values of *M* or *N*. Also, the heat transfer intensity from the wall to the micropolar fluid is maximized for increasing values of *X*, and decreases as *X* decreases. Fig. 11b reveals that the isotherms are departing from the hot wall for greater values of *M* and becoming closer to the hot wall as *N* increases. The fluid flow with heat transfer visualization can be appraised with the aid of heat lines as shown in Fig. 11c. The heat lines illustrate the heat extraction from a hot cylindrical wall in the boundary layer region. The heat function contours indicate bordered corridors and are efficient tools for the heat transfer flow visualization and examination, rather than only streamlines and isotherms. Additionally as the magnetic parameter *M* increases, the maximum value of Ω decreases, since $\overline{Nu}$ decreases on the hot wall as shown in **Table 5**. As *M* or *N* are increased, these heat lines move away from the hot wall. As *N* increases the maximum value of the heat function (Ω) increases since $\overline{Nu}$ increases (**Table 5**). Finally, it is concluded that the heat lines occur in the neighborhood of the hot cylindrical wall i.e. near to thermal boundary layer as assumed by the boundary layer theory hypothesis.

Figure 12 illustrates the time-independent heat lines for different values of *K* with fixed values of other physical parameters. It is evident that the amount of the heat transfer from the hot cylindrical wall to the fluid is a maximum for rising values of *X*, and it is reduced as *X* decreases. The main observation in this figure is the significant heat transfer processes that take place in proximity to the hot cylindrical wall, as presumed by the boundary-layer theory. The heatlines are observed to migrate slightly away from the hot wall with an elevation in micropolar vortex viscosity parameter,

K. Also, it is seen that as *K* upsurges the peak value of the heat function (Ω) decreases since the average heat transport coefficient is reduced on the hot wall. Further, it is noticed that the heatlines occur very close to the hot cylindrical wall. However this behaviour is not exhibited in the case of streamlines.

4.4 Comparison between micropolar and Newtonian fluid flows

Figures 13a, b illustrate the U, θ and S contours for micropolar and Newtonian fluid cases, respectively. The influence of K on the flow-field variable contours is revealed in Fig. 13. As K decreases the velocity and micro-rotation contours tend to move away from the hot wall, while the opposite trend is computed in the temperature distribution. In the boundary layer region of the hot cylindrical wall, with increasing value of K, the variation in the velocity contour levels is reduced and the opposite trend is noted in the case of the isotherms and micro-rotation contours. Further, it is identified that the deviation of velocity and micro-rotation contours of the Newtonian fluid ($K = 0$) from a hot wall exhibit greater magnitudes compared with those of a micropolar fluid ($K > 0$) and for temperature contours, the converse trend is computed. Also, at any given location in the 2D-rectangular region i.e. $0 < X \leq 1.0, 1 < R \leq 1.12$, the velocity of the micropolar fluid flow is observed to be smaller than the Newtonian fluid flow. However, for the temperature and micro-rotation the reverse trend is observed at any location in the (X, R) coordinate system except at the boundary points ($X = 0$, $R = 1$ & $R = 20$). Also, the time-independent state temperature contours for micropolar fluid are slightly different with thicker thermal boundary layer than for a Newtonian fluid.

Table 4 tabulates differences between micropolar and Newtonian fluid flows for the flow-field variables with their temporal peak and the time-independent state values for different M and N. For all values of M and N, the time required for U, θ and S to attain the steady-state for the micropolar fluid ($K > 0$) is less than for a Newtonian fluid ($K = 0$). Also, the peak velocity values occurring at $X = 1.0$ for micropolar fluid are smaller compared with those of a Newtonian fluid.

Table 5 tabulates the differences between micropolar and Newtonian fluids about the average momentum and heat transport coefficients. The values of these coefficients for a micropolar fluid ($K > 0$) are of lower magnitude compared with a Newtonian fluid ($K = 0$). Thus, the characteristics of average momentum and heat transport coefficients of micropolar fluids significantly vary from those of Newtonian fluids, indicating that the presence of suspensions (micro-elements) which characterize real rheological materials exerts a non-trivial contribution.

5. CONCLUDING REMARKS

A numerical study has been conducted to evaluate the thermo-fluid characteristics of transient two-dimensional laminar buoyancy-driven hydromagnetic micropolar fluid flow from a radiating slender cylinder with Bejan's heat line concept. This study has been motivated by further elaborating the thermal and hydrodynamic characteristics of certain magnetic high-temperature enrobing processes which are being deployed in the aerospace and automotive engineering sectors. The Crank-Nicolson computational method has been applied to solve the normalized transport equations. The computations are carried out for different values of magnetic parameter, M (= 1.0, 2.0 and 3.0) and conduction-radiation parameter N (= 2.0, 5.0 and 15). It is observed that with increasing values of M or N, the time elapsed to reach the steady-state *increases* for velocity and temperature profiles. However as M or N increase the velocity decreases i.e. the boundary layer

flow is decelerated and linear momentum boundary layer thickness is increased. With increasing *M*, the temperature increases owing to the supplementary work expended in dragging the micropolar fluid against the action of the transverse magnetic field which is dissipated as thermal energy (heat). Furthermore skin friction and Nusselt number ($\overline{C_f}$ and $\overline{Nu}$) both decrease as *M* increases which is attributable to the deceleration in the flow and the provision of extra heat resulting from the inhibiting action of the magnetic field. The deviations of velocity, temperature and micro-rotation profiles of micropolar fluid flow from those of the Newtonian fluid flow turn are also computed to be substantial. Bejan's heat flow concept includes the heat line plots. The physical characteristics of heat lines are an excellent aid in evaluating thermal convection physics and achieving heat transfer visualization in the entire two-dimensional domain. Also in a given rectangular region, the heat lines provide a robust approach for assessing the heat transfer rate at all levels. The employed non-dimensional thermal radiative heat function is closely related to the average heat transport coefficient on the hot cylindrical wall and characterizes the overall heat transfer rate process from the hot wall to the cold wall. It is noticed that as *M* or *N* increases, the heat lines move away from the hot wall. Also, as *N* is increased, the maximum value of Ω increases and the opposite trend is generated with increasing *M*. Further, the heatlines are slightly moving away from the hot wall for amplifying values of *K* . Flow visualization indicates that the heat lines exist in a finite region which is identified to be adjacent to the hot cylindrical wall. Finally, the present simulations have shown that flow profiles, average heat and momentum transport coefficients of the micropolar fluid flow ($K > 0$) deviate noticeably from those of a Newtonian fluid ($K = 0$). Finally, the current work has utilized a simple algebraic radiative flux model, has neglected many magnetohydrodynamic effects and has been confined to the classical Fourier heat conduction model. A possible pathway for future work is to consider a more sophisticated radiative flux model e.g. P1 differential approximation [41], to consider Hall and ionslip current effects [42] and employ a non-Fourier heat conduction model which correctly predicts finite thermo-elastic waves [43].

ACKNOWLEDGEMENTS

The authors wish to express their gratitude to all three reviewers who highlighted important areas for improvement in this article. Their suggestions have served to enhance the clarity and depth of the interpretation in particular.

REFERENCES

[1] Sparrow, E. M., and J. L. Gregg (1956). Laminar free convection heat transfer from the outer surface of a vertical circular cylinder, *ASME Journal of Heat Transfer 78,* 1823-1829.

[2] Lee, H. R., T. S. Chen, and B. F. Armaly (1988). Natural convection along slender vertical cylinder with variable surface temperature, *Journal of Heat Transfer 110*, 103–108.

[3] Miyamoto, M., J. Sumikawa, T. Akiyoshi, and T. Nakamura (1980). Effects of axial heat conduction in a vertical flat plate on free convection heat transfer, *International Journal of Heat and Mass Transfer 23 (11),* 1545–1553.

[4] Pop, I, B. Ingham, and Y. Yuan (1996). Mixed convective conjugate heat transfer from a vertical flat plate, *Journal of Applied Mathematics and Mechanics / Zeitschrift für Angewandte Mathematik und Mechanik 76 (5),* 281–289.

[5] Kaya, A. (2011). Effects of buoyancy and conjugate heat transfer on non-Darcy mixed convection about a vertical slender hollow cylinder embedded in a porous medium with high porosity, *International Journal of Heat and Mass Transfer 54 (4),* 818–825.

[6] Pop, I, and Na TY (2000). Conjugate free convection over a vertical slender hollow cylinder embedded in a porous medium, *Heat Mass Transfer 36,* 375-379.

[7] Rani, H. P., and G. J. Reddy (2013). Soret and Dufour effects on transient double diffusive free convection of couple-stress fluid past a vertical cylinder, *Journal of Applied Fluid Mechanics 6(4),* 545-554.

[8] Hirschhorn, J., M. Madsen, A. Mastroberardino, A. and J.I.Siddique (2016). Magnetohydrodynamic boundary layer slip flow and heat transfer of power law fluid over a flat plate, *Journal of Applied Fluid Mechanics 9(1),* 11-17.

[9] Eringen, A.C. (1966). Theory of micropolar fluids, *Journal of Mathematics and Mechanics 16,* 1-18.

[10] Stokes ,V.K. (1966). Couple stress in fluids, *Physics of Fluids 9,* 1709-1715.

[11] Eringen, A.C. (1972). Theory of thermomicropolar fluids, *Journal of Mathematical Analysis and Applications 38,* 481–496.

[12] Xinhui Si and Liancun Zheng (2013).The Flow and heat transfer of a micropolar fluid in a porous channel with expanding or contracting walls, *International Journal of Heat and Mass Transfer 67,* 885–895.

[13] Bég, O. Anwar, M. M. Rashidi, T. A. Bég and M. Asadi (2012). Homotopy analysis of transient magneto-bio fluid dynamics of micropolar squeeze film in a porous medium: a model for magneto bio-rheological lubrication, *Journal of Mechanics in Medicine and Biology 12(3),* 1250051.

[14] Misra, J.C., S. Chandra, G. C. Schit, and P. K. Kundu (2014). Electroosmotic oscillatory flow of micropolar fluid in microchannels: application to dynamics of blood flow in microfluidic devices, *Applied Mathematics and Mechanics 35(6),* 749–766.

[15] Hayat, T., T. Javed, and Z. Abbas (2009). MHD flow of a micropolar fluid near a stagnation point towards a non-linear stretching surface, *Nonlinear Analysis: Real World Applications 10,* 1514–1526.

[16] Hayat, T., T. Javed, and Z. Abbas (2010). Corrigendum to MHD flow of a micropolar fluid near a stagnation-point towards a non-linear stretching surface [Nonlinear Anal. RWA 10 (2009) 1514 - 1526], *Nonlinear Analysis: Real World Applications 11,* 2190.

[17] Manzari, M.T. (2004). Application of micropolar plasticity to post failure analysis in geomechanics, *International Journal for Numerical Analytical Methods in Geomechanics 28*, 1011–1032.

[18] Prathap Kumar, J., J.C. Umavathi, Ali J. Chamkha and Ioan Pop (2010). Fully-developed free-convective flow of micropolar and viscous fluids in a vertical channel, *Applied Mathematical Modelling 34,* 1175–1186.

[19] Ariman, T., Turk MA and Sylvester ND (1974). Applications of microcontinuum fluid mechanics, *International Journal of Engineering Science 12(4),* 273-293.

[20] Tetbirt, T., M.N. Bouaziz, and M. Tahar Abbes (2016). Numerical study of magnetic effect on the velocity distribution field in a macro/micro-scale of a micropolar and viscous fluid in vertical channel, *Journal of Molecular Liquids 216,* 103–110.

[21] Kimura, S. and A. Bejan (1983). The heat line visualization of convective heat transfer, *ASME Journal of Heat Transfer 105,* 916 – 919.

[22] Bejan, A. (1984).*Convection Heat Transfer, 1st ed., Wiley, New York: John Wiley and Sons.*

[23] Mahmud, S., and R. Fraser (2007). Visualizing energy flows through energy streamlines and pathlines, *International Journal of Heat and Mass Transfer 50 (19)*, 3990-4002.

[24] Hooman, K. (2010). Energy flux vectors as a new tool for convection visualization, *International Journal of Numerical Methods for Heat and Fluid Flow 20 (2)*, 240–249.

[25] Mahapatra, P.S., A. Mukhopadhyay, N.K. Manna, K. Ghosh (2018). Heatlines and other visualization techniques for confined heat transfer systems, *International Journal of Heat and Mass Transfer 118,* 1069-1079.

[26] Mahapatra,P.S., N.K. Manna, K. Ghosh, A. Mukhopadhyay (2015). Heat transfer assessment of an alternately active bi-heater undergoing transient natural convection, *International Journal of Heat and Mass Transfer 83*, 450-464.

[27] Aggarwal, S. and A. Manhapra (1989). Transient natural convection in a cylindrical enclosure non uniformly heated at the top wall, *Numerical Heat Transfer Part A. 15,* 341–356.

[28] Rani, H. P., and G. J. Reddy (2013). Heatline visualization for conjugate heat transfer of a couple stress fluid from a vertical slender hollow cylinder, *International Communications in Heat and Mass Transfer 48*, 46–52.

[29] Rani, H. P., G. Janardhana Reddy, Chang Nyung Kim, and Y. Rameshwar (2015). Transient couple stress fluid past a vertical cylinder with Bejan's heat and mass flow visualization for steady-state, *ASME Journal of Heat Transfer 137,* 032501–12.

[30] Das, D., and T. Basak (2016). Analysis of average Nusselt numbers at various zones for heat flow visualizations during natural convection within enclosures (square vs. triangular) involving discrete heaters, *International Communications in Heat and Mass Transfer 75*, 303-310.

[31] Morega, A.M. (1988). The heat function approach to the thermomagnetic convection of electroconductive melts, *Revue roumaine des Sciences Techniques. Electrotechnique et energetique, Part II, 33*, 155-166.

[32] Morega, A.M. (1988). Magnetic field influence on the convective heat transfer in the solidification processes, *Revue roumaine des Sciences Techniques. Electrotechnique et energetique 33*, 155-166.

[33] Mahapatra, P.S., N.K. Manna, K. Ghosh, A. Mukhopadhyay (2015). Heat transfer assessment of an alternately active bi-heater undergoing transient natural convection, *International Journal of Heat and Mass Transfer 83*, 450-464.

[34] Mahapatra, P.S., A. Mukhopadhyay, N.K. Manna, (2018). Ghosh, Heatlines and other visualization techniques for confined heat transfer systems, *International Journal of Heat and Mass Transfer 118, 1069-1079.*

[35] Nirmalendu biswas and Nirmal k manna (2017). Transport phenomena in a sidewall-moving bottom-heated cavity using heatlines, *Sadhana 42(2)*,193–211.

[36] Brewster, M.Q. (1992). *Thermal Radiative Transfer and Properties*, John Wiley Sons, New York, USA.

[37] Chang, C. (2006). Buoyancy and wall conduction effects on forced convection of micropolar fluid flow along a vertical slender hollow circular cylinder, *International Journal of Heat and Mass Transfer 49*, 4932–4942.

[38] Rani, H. P., G. J. Reddy, and C.N. Kim (2013). Transient analysis of diffusive chemical reactive species for couple stress fluid flow over vertical cylinder, *Applied Mathematics and Mechanics 34*, 985-1000.

[39] Heckel, J. J., T. S. Chen, and B.F. Armaly (1989). Mixed convection along slender vertical cylinders with variable surface temperature, *International Journal of Heat and Mass Transfer*

32, 1431–1442.

[40] Aggarwal, S. and A. Manhapra (1989). Use of heat lines for unsteady buoyancy-driven flow in a cylindrical enclosure, *ASME Journal of Heat Transfer 111*, 576–578.

[41] Bég, O. Anwar, N. Ali, A. Zaman, Eemaan T. A. Bég and Ayesha Sohail (2016). Computational modelling of heat transfer in annular porous medium solar energy absorber with a P1-radiative differential approximation, *Journal of the Taiwan Institute of Chemical Engineers 66,* 258-268.

[42] Bég, O. Anwar, J. Zueco and H.S. Takhar (2009). Unsteady magnetohydrodynamic Hartmann–Couette flow and heat transfer in a Darcian channel with Hall current, ionslip, viscous and Joule heating effects: Network numerical solutions, *Communications in Nonlinear Science Numerical Simulation 14,* 1082-1097.

[43] Bhatti M.M., A. Shahid, Bég, O. Anwar and A. Kadir (2017). Numerical study of radiative Maxwell viscoelastic magnetized flow from a stretching permeable sheet with the Cattaneo–Christov heat flux model, *Neural Computing and Applications,* 1-12. doi.org/10.1007/s00521-017-2933-8

TABLES

Table 1. Grid independence test for selecting mesh size.

Grid size	$\overline{C_f}$ for Pr = 0.7, Gr = 10^6, P = 0.5, K = 1.2, M = 2.0 and N = 2.0.	$\overline{Nu}$ for Pr = 0.7, Gr =10^6, P = 0.5, K = 1.2, M = 2.0 and N = 2.0.
20 X 120	3.1548	6.3239
30 X 180	3.3992	6.5121
40 X 240	3.8032	6.9215
50 X 300	3.8147	6.9636
60 X 360	3.8149	6.9639

Table 2. Grid independence test for selecting time step size.

Time step size (Δt)	$\overline{C_f}$ for Pr = 0.7, Gr = 10^6, P = 0.5, K = 1.2, M = 2.0 and N = 2.0.	$\overline{Nu}$ for Pr = 0.7, Gr =10^6, P = 0.5, K = 1.2, M = 2.0 and N = 2.0.
0.5	3.8151	6.9631
0.1	3.8148	6.9634
0.08	3.8148	6.9634
0.05	3.8148	6.9634
0.02	3.8148	6.9634
0.01	3.8147	6.9636

Table 3. Comparison of local heat transport coefficient with $P = 0.0$, $M = 0.0$, $N = 0.0$, $K = 0.0$ and $Gr = 10^5$ at $X = 0.05$.

Pr	0.7	7.0
Present	0.7858	1.1608
Heckel *et al.* [39]	0.7820	1.1609

Table 4. The time required for various flow-field variables to attain the temporal peak and the time-independent state; the peak velocity for various M and N with $P = 0.5$, $Pr = 0.7$ and $Gr = 10^6$ for (a) micropolar fluid ($K = 1.2$); (b) Newtonian fluid ($K = 0.0$).

M	N	Temporal peak time (t) of $U(1, 1.16)$	$\theta(1, 1.16)$	steady-state time (t)	Peak velocity (U) at $X = 1.0$
(a) Micropolar fluid ($K = 1.2$)					
1.0	2.0	15.58	14.98	32.65	0.1309
1.0	5.0	17.23	16.63	32.89	0.1180
1.0	15.0	18.37	17.70	33.00	0.1112
2.0	2.0	-	-	48.59	0.0941
3.0	2.0	-	-	50.00	0.0749
(b) Newtonian fluid ($K = 0.0$)					
1.0	2.0	15.32	14.90	32.73	0.1364
1.0	5.0	16.58	16.50	33.05	0.1228
1.0	15.0	17.74	17.58	33.22	0.1158
2.0	2.0	-	-	48.60	0.0965
3.0	2.0	-	-	50.10	0.0761

Table 5. Comparison between the (a) micropolar fluid (K = 1.2) and (b) Newtonian fluid (K = 0.0) flows for various values of M and N regarding the average values of $\overline{C_f}$ and $\overline{Nu}$ with Pr = 0.7, P = 0.5 and $Gr = 10^5$.

	M	N	$\overline{C_f}$	$\overline{Nu}$
(a) Micropolar fluid (K = 1.2)				
	1.0	2.0	4.4545	7.9238
	1.0	5.0	4 .0914	8.6184
	1.0	15.0	3.9018	9.0217
	2.0	2.0	3.8147	6.9636
	3.0	2.0	3.4110	6.3388
(b) Newtonian fluid (K = 0.0)				
	1.0	2.0	5.0874	8.1112
	1.0	5.0	4.6732	8.8380
	1.0	15.0	4.4570	9.2607
	2.0	2.0	4.3009	7.0909
	3.0	2.0	3.8087	6.4335

FIGURES

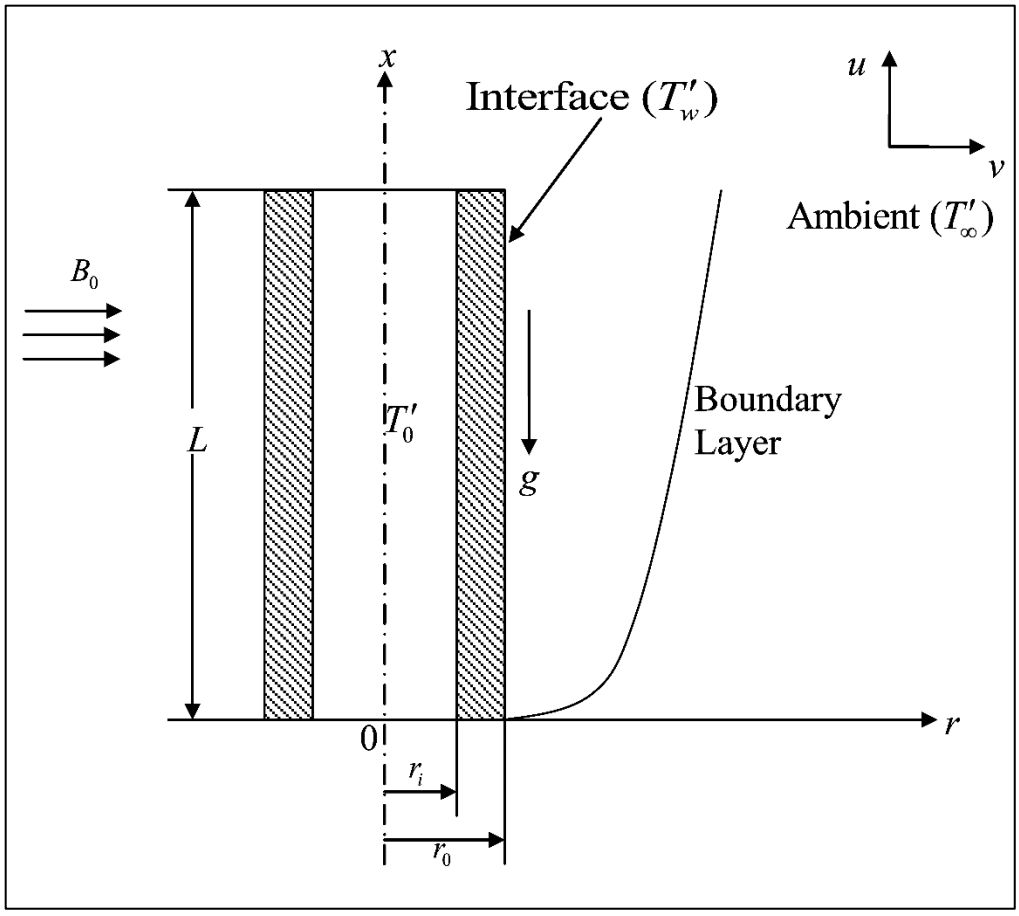

Fig. 1. Flow geometry and cylindrical coordinate system.

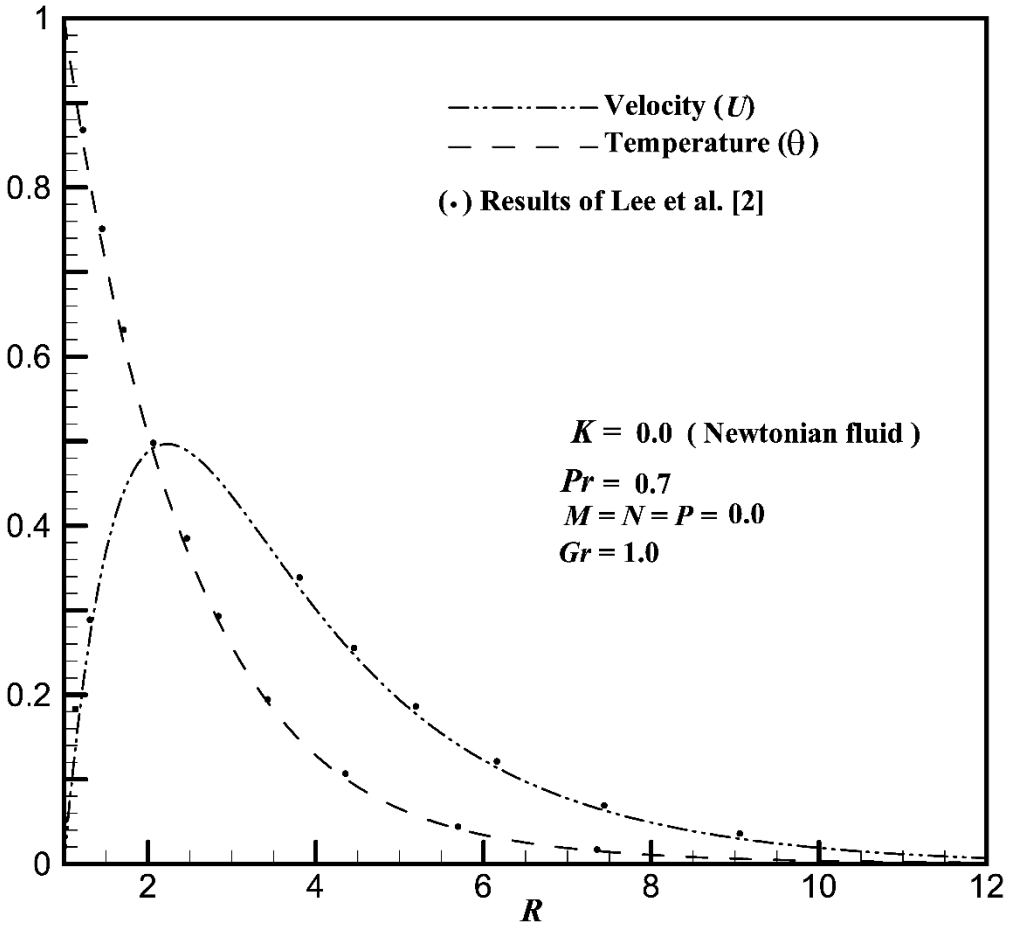

Fig. 2. Comparison of flow-field variables.

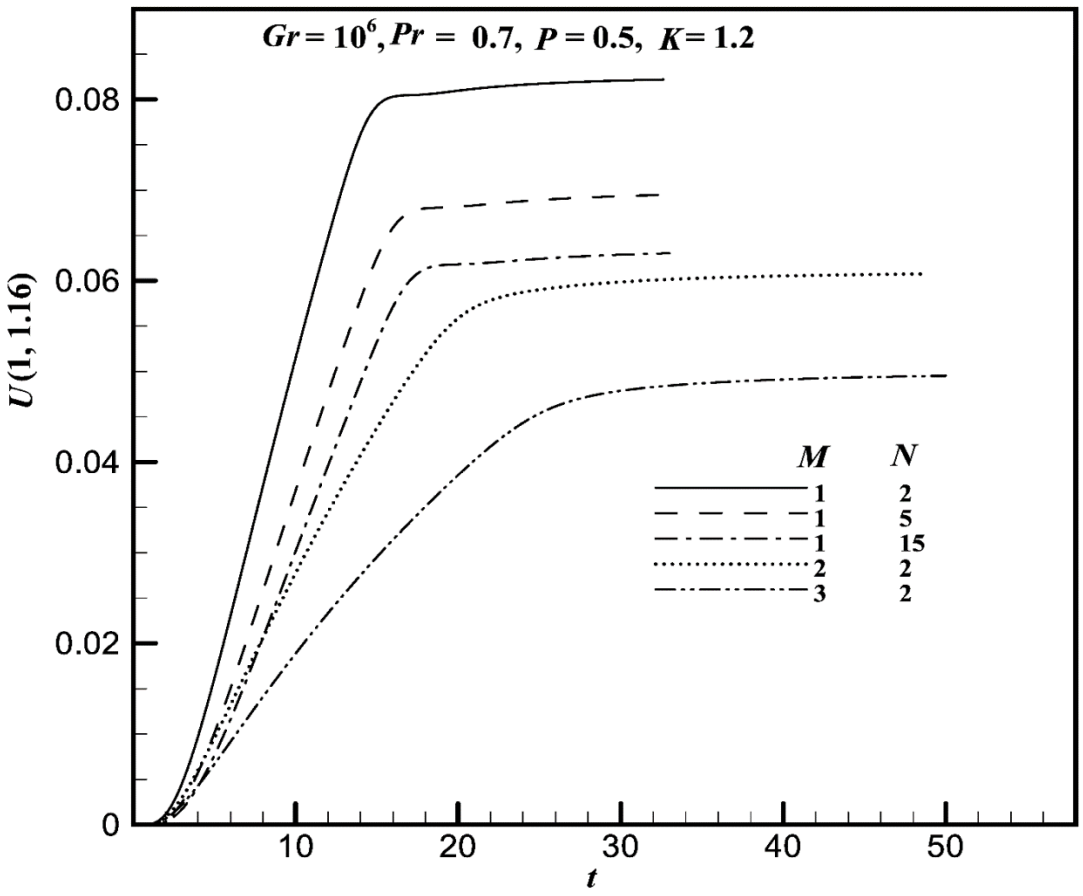

Fig. 3. Time-dependent velocity profile (U) versus time (t) at the point (1, 1.16) for the effect of M and N.

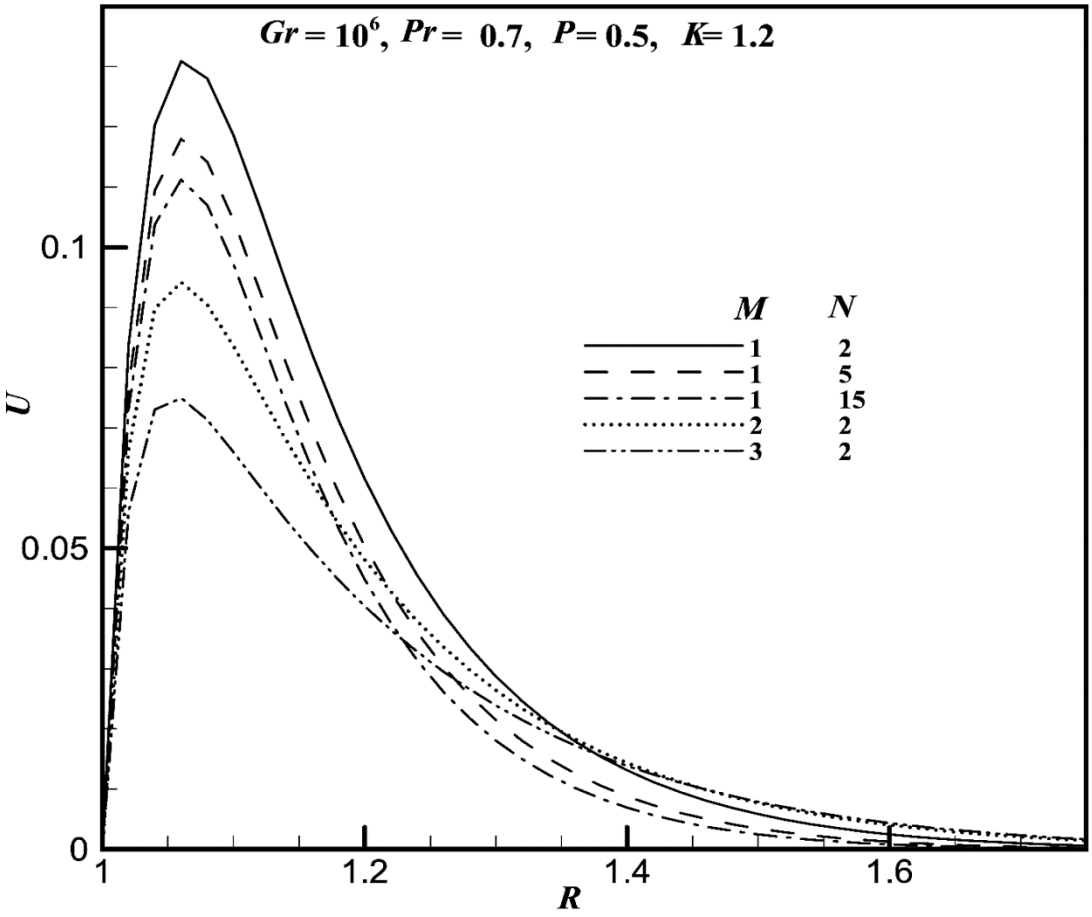

Fig. 4. Simulated time-independent state velocity profile (U) versus R at X = 1.0 for the effect of M and N.

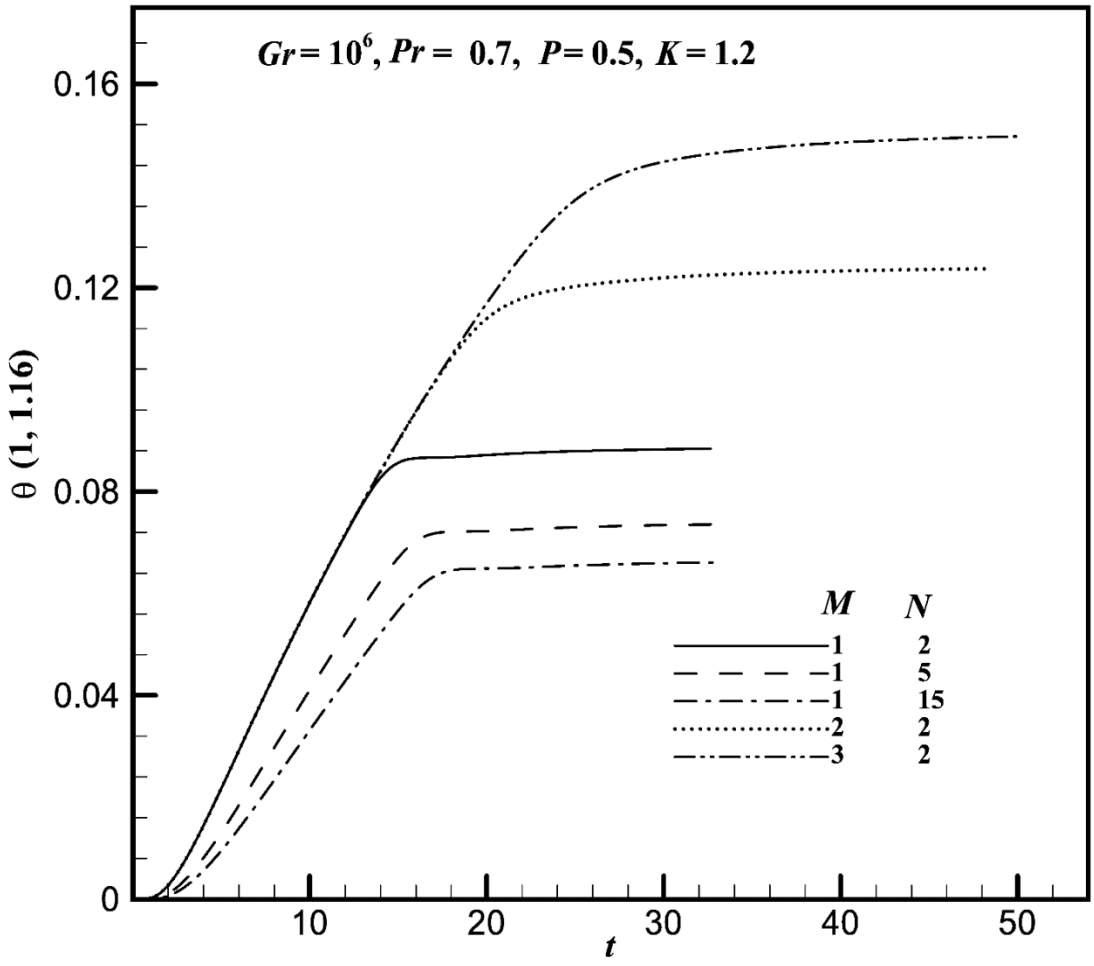

Fig. 5. Simulated time-dependent temperature profile (θ) versus time (*t*) at the point (1, 1.16) for the effect of *M* and *N*.

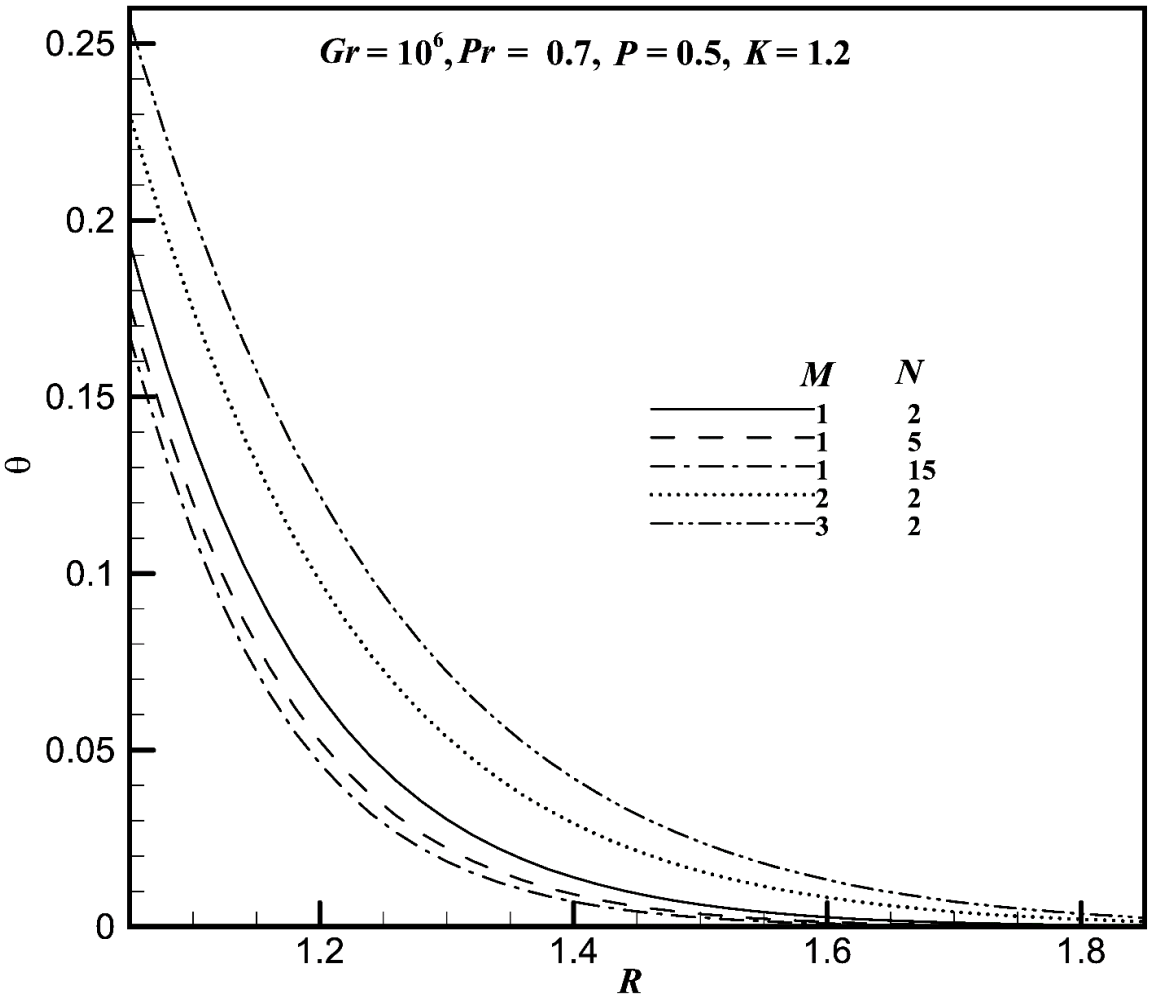

Fig. 6. Time-independent state temperature profile (θ) versus *R* at *X* = 1.0 for the effect of *M* and *N*.

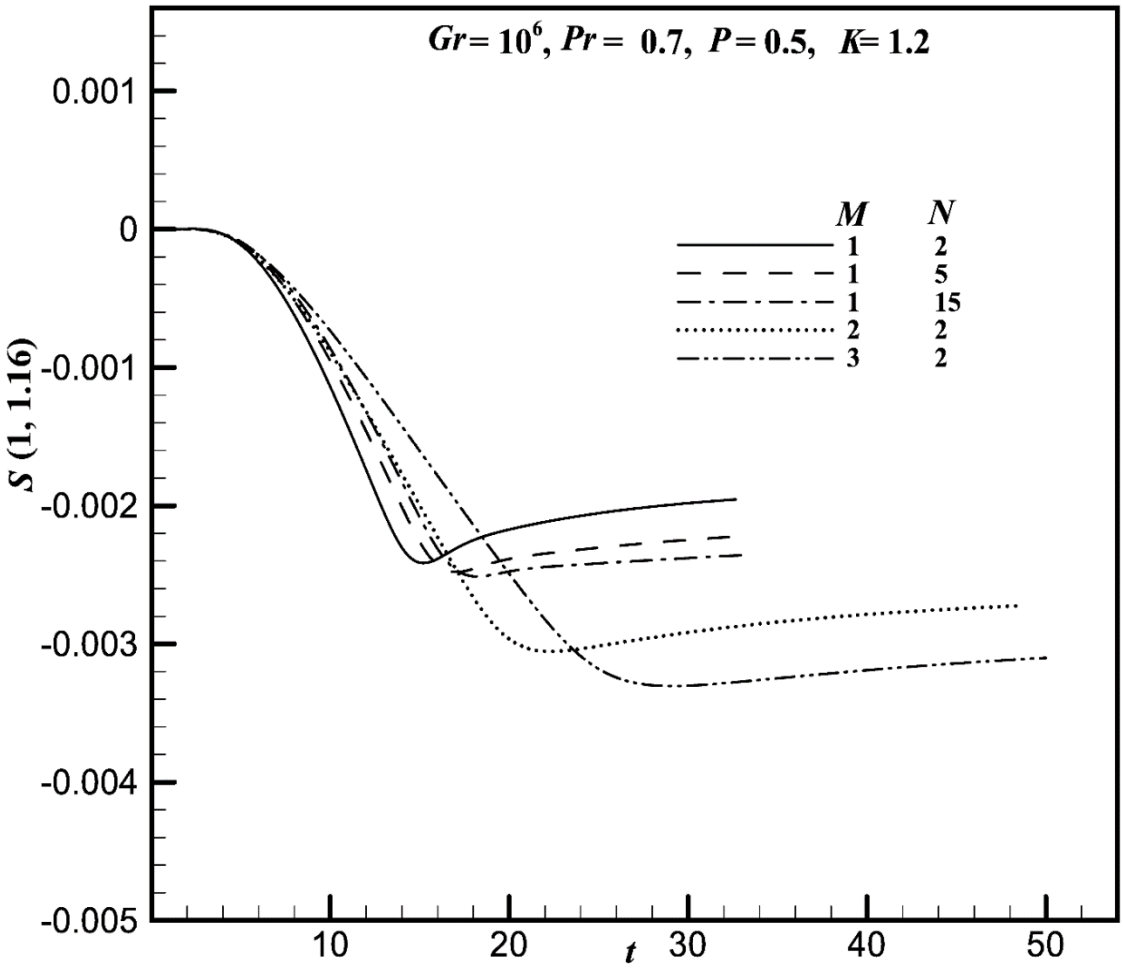

Fig. 7. Time-dependent microrotation (*S*) profile at the point (1, 1.16) for the effect of *M* and *N*.

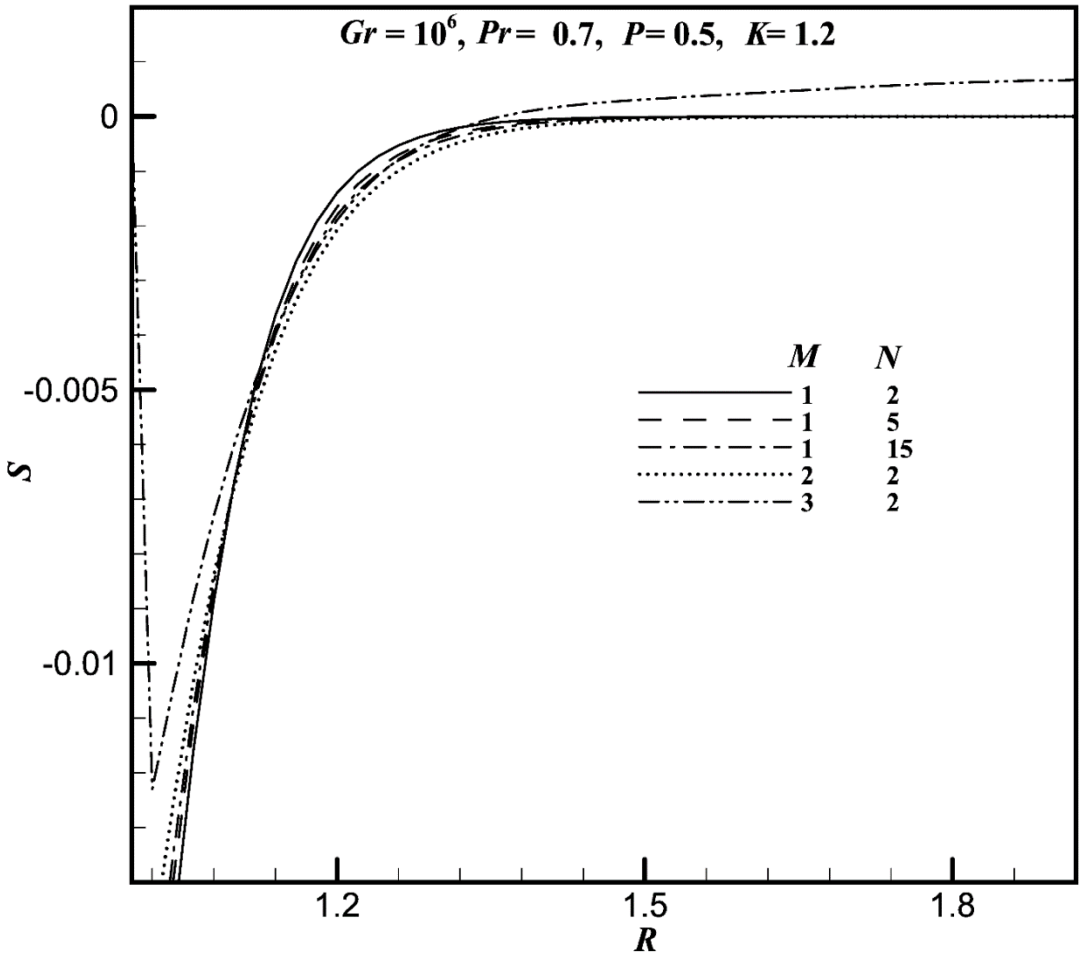

Fig. 8. Simulated time-independent state microrotation (S) profile against R at X = 1.0 for the effect of M and N.

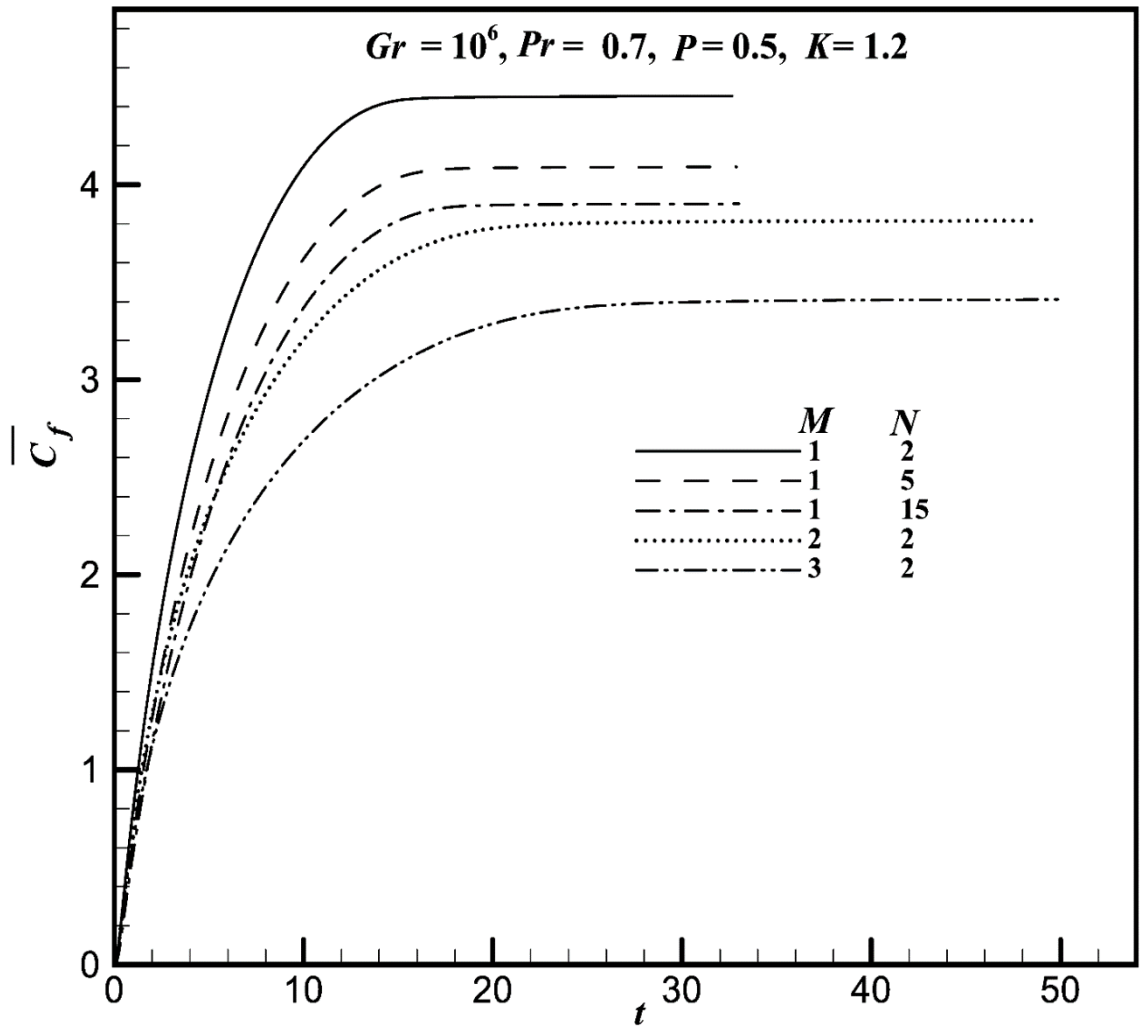

Fig. 9. Average momentum transport coefficient ($\overline{C_f}$) profile against *t* for the effect of *M* and *N*.

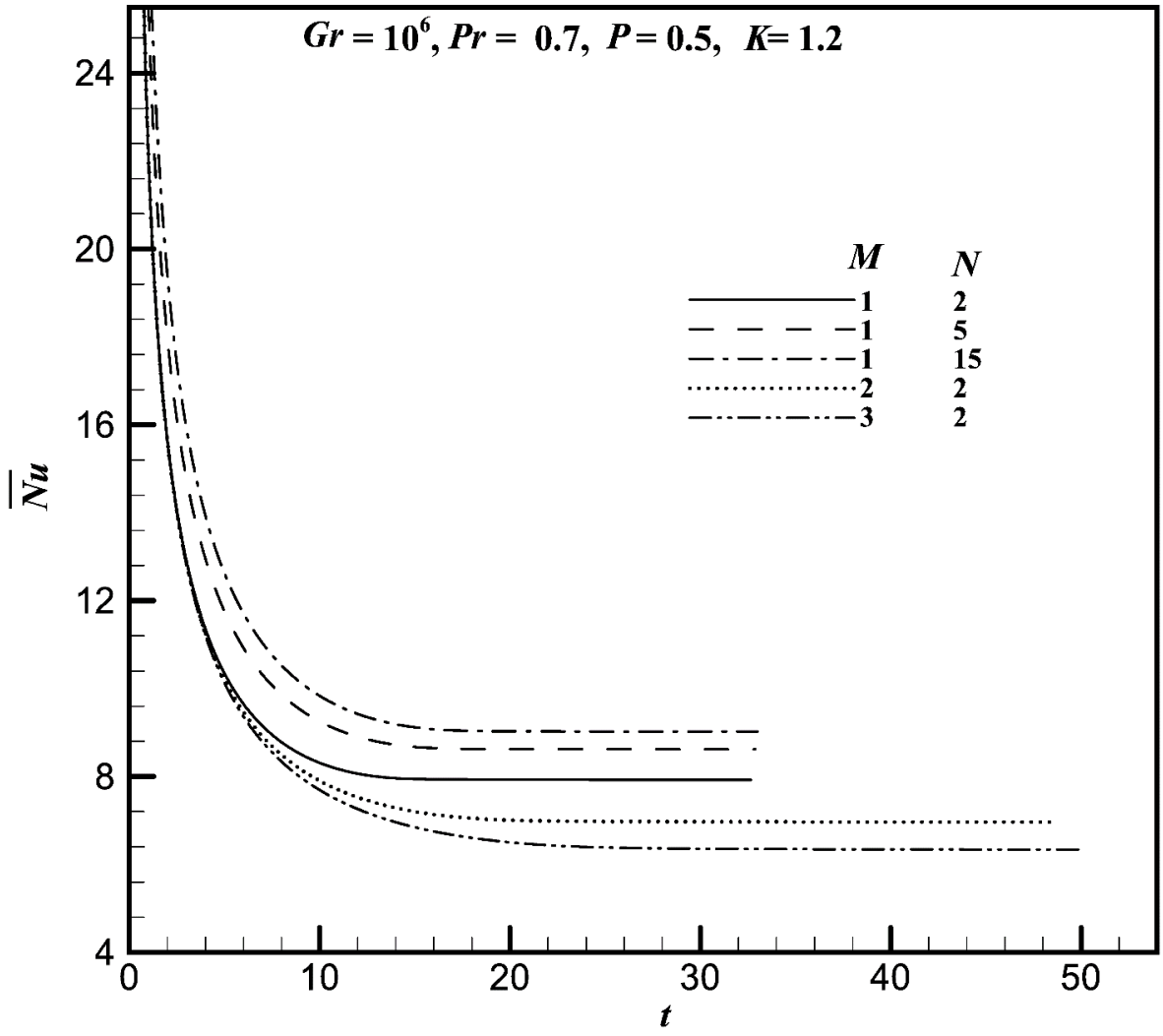

Fig. 10. Average heat transport coefficient ($\overline{Nu}$) profile against *t* for the effect of *M* and *N*.

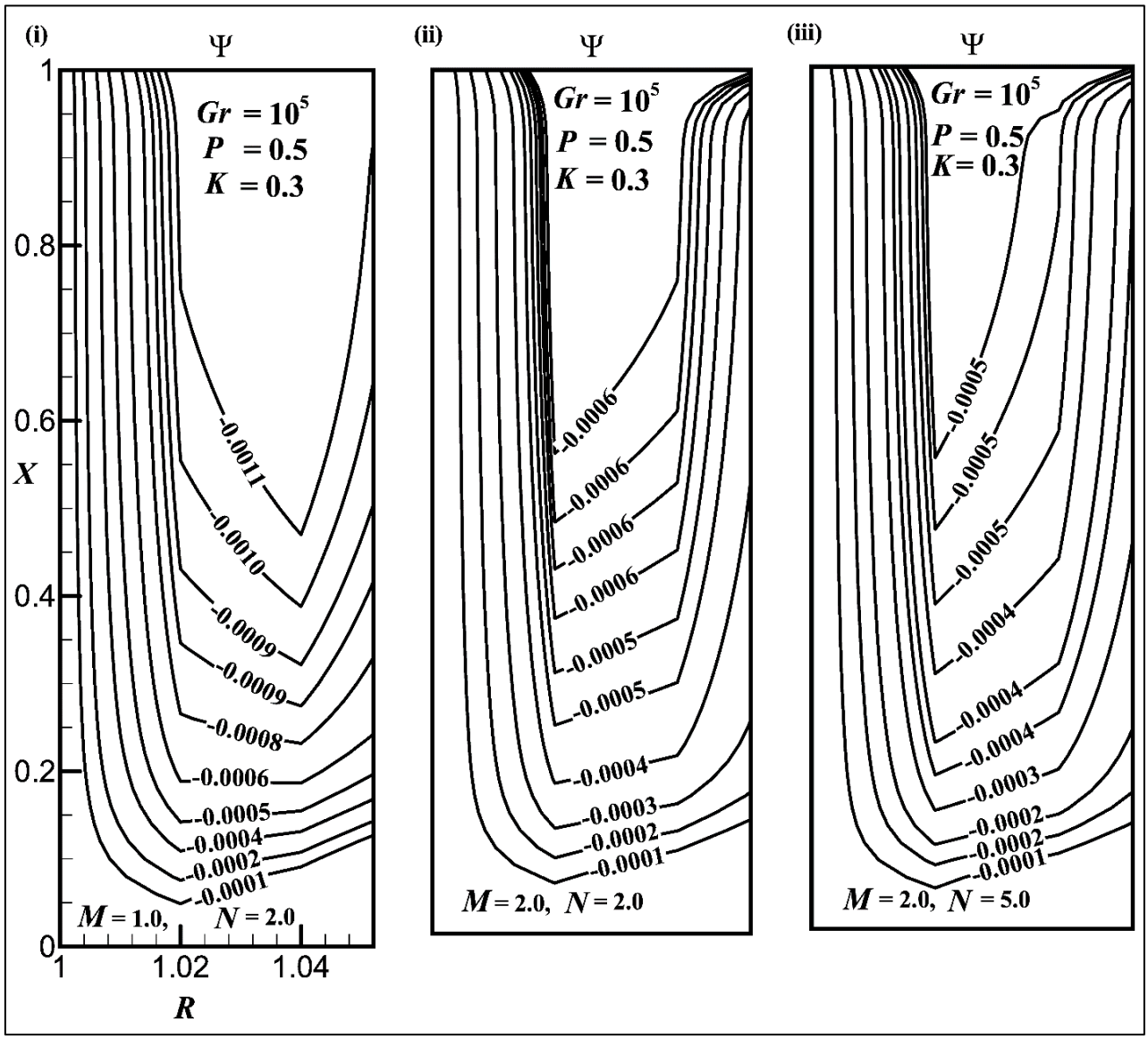
(i)
Ψ
Gr = 10^5
P = 0.5
K = 0.3
-0.0011
-0.0010
-0.0009
-0.0009
-0.0008
-0.0006
-0.0005
-0.0004
-0.0002
-0.0001
M = 1.0, N = 2.0
X
R
0
0.2
0.4
0.6
0.8
1
1
1.02
1.04
(ii)
Ψ
Gr = 10^5
P = 0.5
K = 0.3
-0.0006
-0.0006
-0.0006
-0.0006
-0.0005
-0.0005
-0.0004
-0.0003
-0.0002
-0.0001
M = 2.0, N = 2.0
(iii)
Ψ
Gr = 10^5
P = 0.5
K = 0.3
-0.0005
-0.0005
-0.0005
-0.0004
-0.0004
-0.0004
-0.0003
-0.0002
-0.0002
-0.0001
M = 2.0, N = 5.0

(11a)

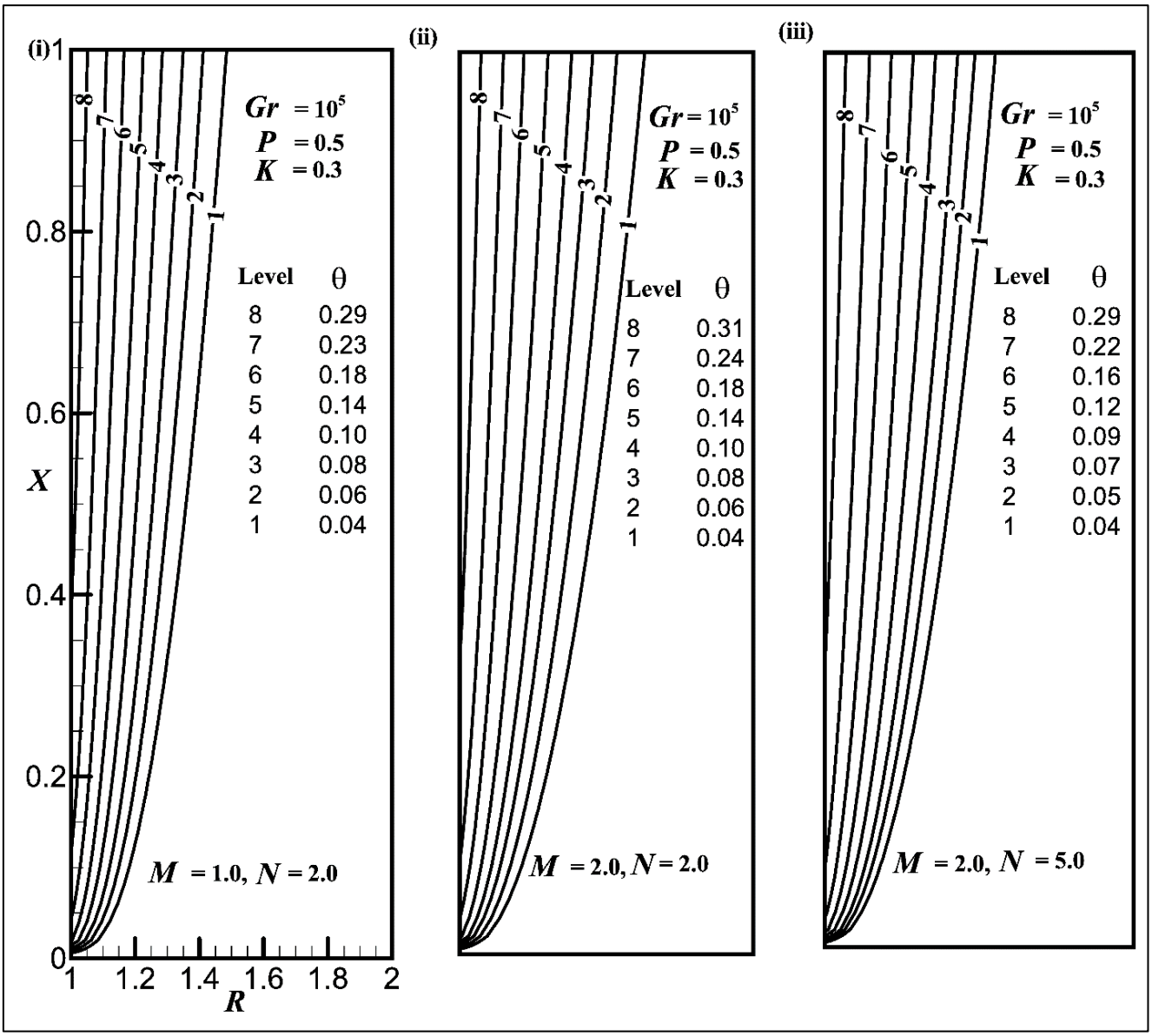
(i)
(ii)
(iii)
Gr = 10^5
P = 0.5
K = 0.3
Level θ
8 0.29
7 0.23
6 0.18
5 0.14
4 0.10
3 0.08
2 0.06
1 0.04
M = 1.0, N = 2.0
Gr = 10^5
P = 0.5
K = 0.3
Level θ
8 0.31
7 0.24
6 0.18
5 0.14
4 0.10
3 0.08
2 0.06
1 0.04
M = 2.0, N = 2.0
Gr = 10^5
P = 0.5
K = 0.3
Level θ
8 0.29
7 0.22
6 0.16
5 0.12
4 0.09
3 0.07
2 0.05
1 0.04
M = 2.0, N = 5.0
X
R
0
0.2
0.4
0.6
0.8
1
1 1.2 1.4 1.6 1.8 2

(11b)

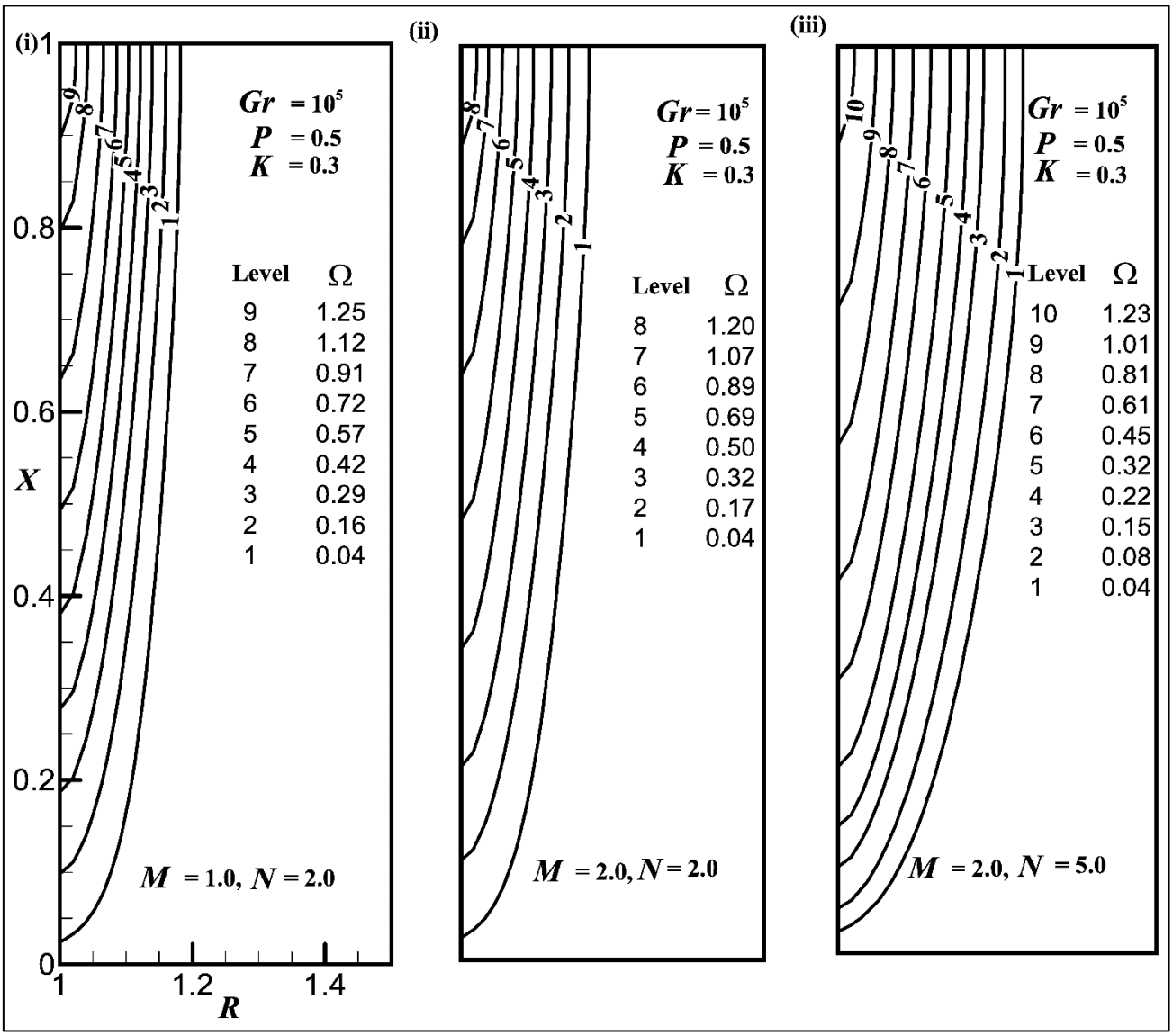

(11c)

Fig. 11. Time-independent state (a) streamlines (ψ); (b) isotherms (θ); and (c) heatlines (Ω) for various values of *M* and *N*.

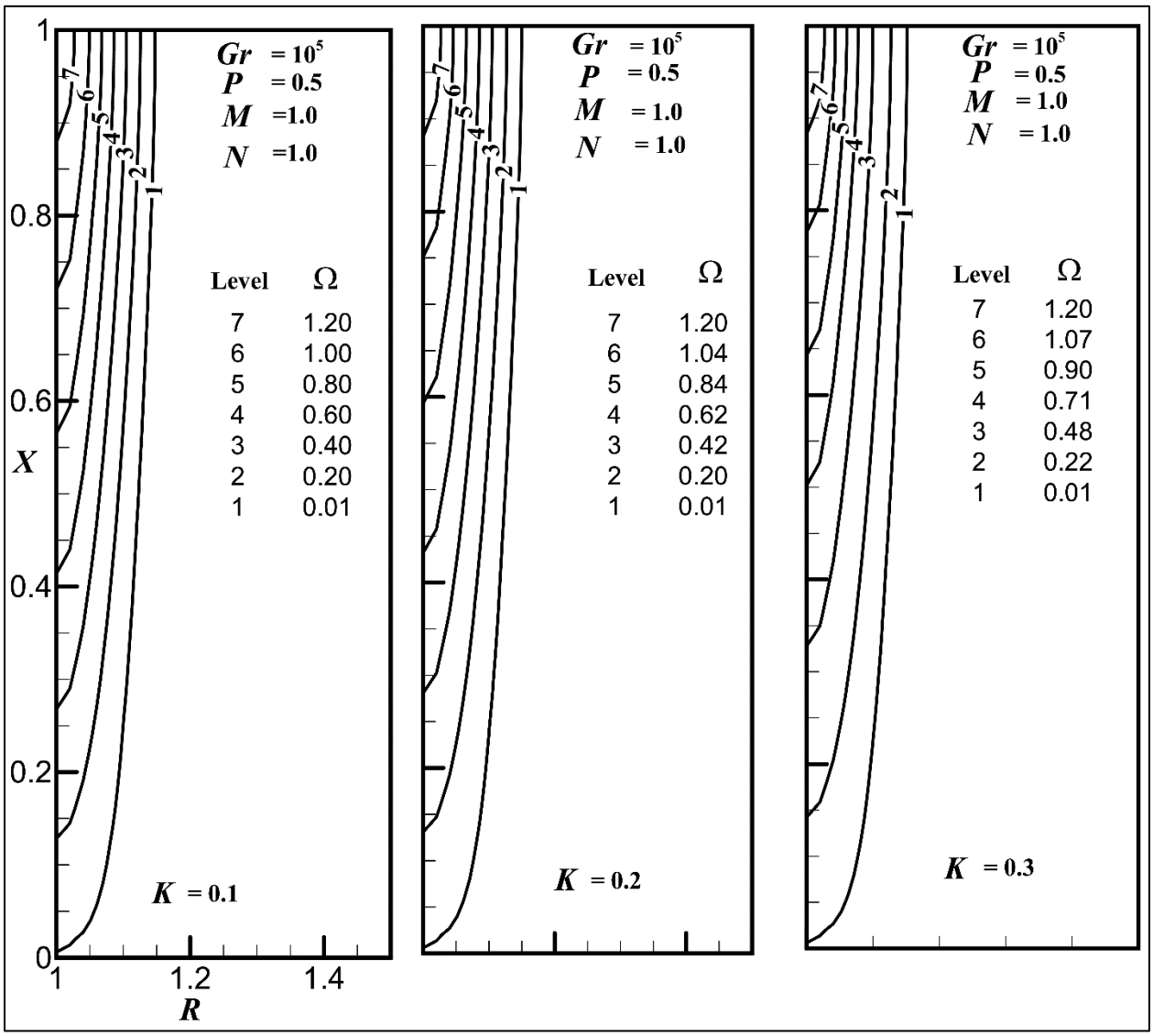

Fig. 12. Time-independent state heat lines (Ω) for various values of K .

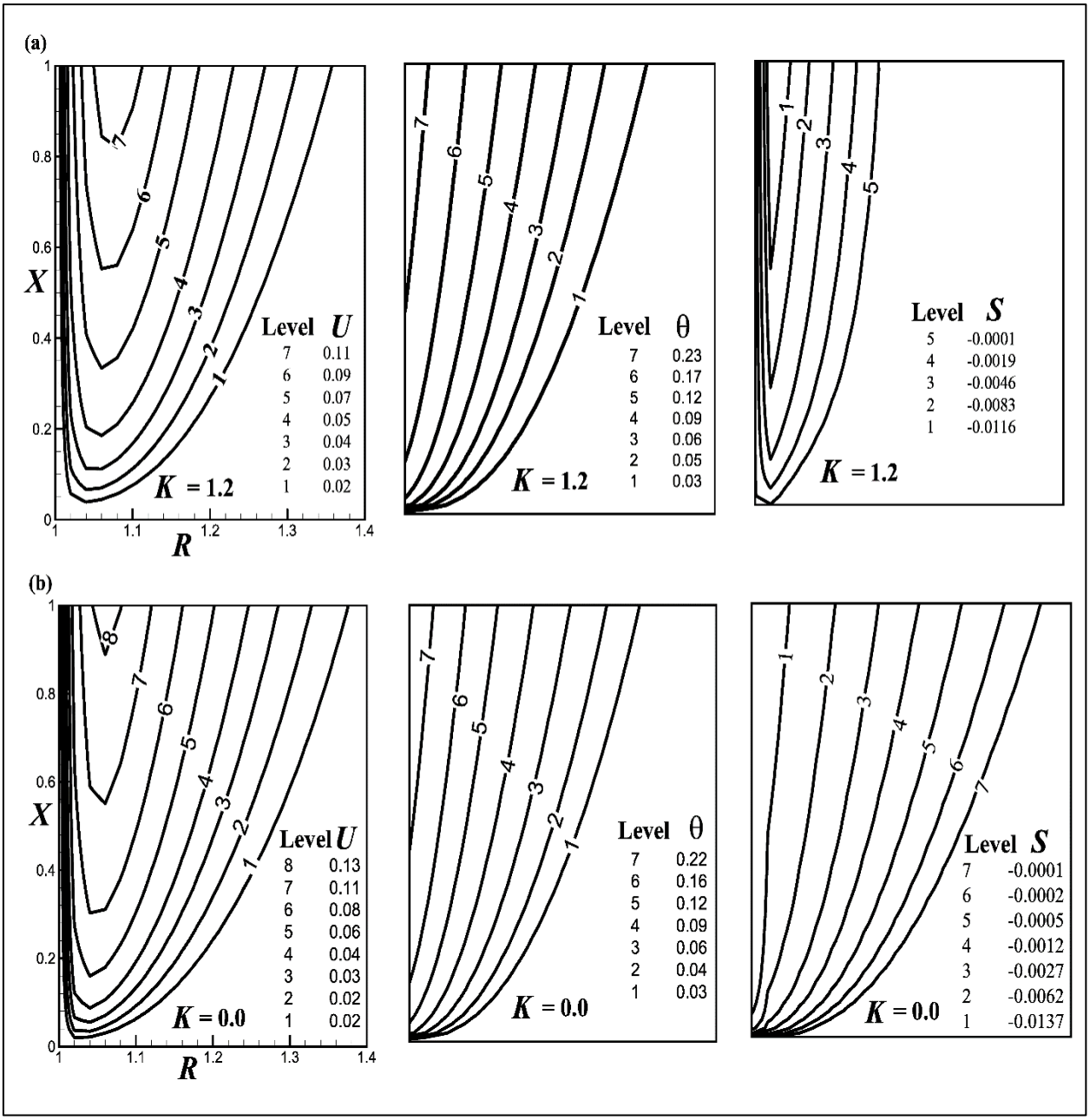

Fig. 13. Time-independent state contours of velocity (*U*), temperature (θ) and microrotation (*S*) for (a) micropolar fluid (*K* = 1.2); & (b) Newtonian fluid (*K* = 0.0).